UPPSALA
UNIVERSITET

Digital Comprehensive Summaries of Uppsala Dissertations from the Faculty of Science and Technology 975

Creating and Probing Extreme States of Materials: From Gases and Clusters to Biosamples and Solids

BIANCA IWAN

ACTA
UNIVERSITATIS
UPSALIENSIS
UPPSALA
2012

ISSN 1651-6214
ISBN 978-91-554-8477-4
urn:nbn:se:uu:diva-180997

Dissertation presented at Uppsala University to be publicly examined in A1:107, Biomedical Center (BMC), Husargatan 3, Uppsala, Friday, November 9, 2012 at 09:00 for the degree of Doctor of Philosophy. The examination will be conducted in English.

Abstract

Iwan, B. 2012. Creating and Probing Extreme States of Materials: From Gases and Clusters to Biosamples and Solids. Acta Universitatis Upsaliensis. *Digital Comprehensive Summaries of Uppsala Dissertations from the Faculty of Science and Technology* 975. 66 pp. Uppsala. ISBN 978-91-554-8477-4.

Free-electron lasers provide high intensity pulses with femtosecond duration and are ideal tools in the investigation of ultrafast processes in materials. Illumination of any material with such pulses creates extreme conditions that drive the sample far from equilibrium and rapidly convert it into high temperature plasma. The dynamics of this transition is not fully understood and the main goal of this thesis is to further our knowledge in this area.

We exposed a variety of materials to X-ray pulses of intensities from 10^{13} to above 10^{17} W/cm^2. We found that the temporal evolution of the resulting plasmas depends strongly on the wavelength and pulse intensity, as well as on material related parameters, such as size, density, and composition.

In experiments on atomic and molecular clusters, we find that cluster size and sample composition influence the destruction pathway. In small clusters a rapid Coulomb explosion takes place while larger clusters undergo a hydrodynamic expansion. We have characterized this transition in methane clusters and discovered a strong isotope effect that promotes the acceleration of deuterium ions relative to hydrogen. Our results also show that ions escaping from exploding xenon clusters are accelerated to several keV energies.

Virus particles represent a transition between hetero-nuclear clusters and complex biological materials. We injected single mimivirus particles into the pulse train of an X-ray laser, and recorded coherent diffraction images simultaneously with the fragmentation patterns of the individual particles. We used these results to test theoretical damage models. Correlation between the diffraction patterns and sample fragmentation shows how damage develops after the intense pulse has left the sample.

Moving from sub-micron objects to bulk materials gave rise to new phenomena. Our experiments with high-intensity X-ray pulses on bulk, metallic samples show the development of a transient X-ray transparency. We also describe the saturation of photoabsorption during ablation of vanadium and niobium samples.

Photon science with extremely strong X-ray pulses is in its infancy today and will require much more effort to gain more knowledge. The work described in this thesis represents some of the first results in this area.

Keywords: free-electron laser, ultrashort X-rays, non-equilibrium plasma, Coulomb explosion, isotope effect, hydrodynamic expansion, ion acceleration, high intensity lasers, ablation, time-of-flight spectroscopy

Bianca Iwan, Uppsala University, Department of Cell and Molecular Biology, Molecular biophysics, Box 596, SE-751 24 Uppsala, Sweden.

ISSN 1651-6214
ISBN 978-91-554-8477-4
urn:nbn:se:uu:diva-180997 (http://urn.kb.se/resolve?urn=urn:nbn:se:uu:diva-180997)

"Very simple was my explanation, and plausible enough
– as most wrong theories are!"

H. G. Wells, The Time Machine

List of Papers

This thesis is based on the following papers, which are referred to in the text by their Roman numerals.

I **Explosion, ion acceleration, and molecular fragmentation of methane clusters in the pulsed beam of a free-electron laser**
B. Iwan, J. Andreasson, M. Bergh, S. Schorb, H. Thomas, D. Rupp, T. Gorkhover, M. Adolph, T. Möller, J. Hajdu, and N. Tîmneanu
Phys. Rev. A 86, 033201 (2012).

II **TOF-OFF: A method for determining focal positions in tightly focused free-electron laser experiments by measurement of ejected ions**
B. Iwan, J. Andreasson, A. Andrejczuk, E. Abreu, M. Bergh, C. Caleman, A. J. Nelson, S. Bajt, J. Chalupsky, H. N. Chapman, R. R. Fäustlin, V. Hajkova, P. A. Heimann, B. Hjörvarsson, L. Juha, D. Klinger, J. Krzywinski, B. Nagler, G. K. Pálsson, W. Singer, M. M. Seibert, R. Sobierajski, S. Toleikis, T. Tschentscher, S. M. Vinko. R. W. Lee, J. Hajdu, N. Tîmneanu
High Energy Density Phys. 7, 336–342 (2011).

III **Modeling of soft X-ray induced ablation in solids**
B. Iwan, J. Andreasson, E. Abreu, M. Bergh, C. Caleman, J. Hajdu, and N. Tîmneanu
Proc. of SPIE 8077, 807705 (2011).

IV **Saturated ablation in metal hydrides and acceleration of protons and deuterons to keV energies with a soft X-ray laser**
J. Andreasson, **B. Iwan**, A. Andrejczuk, E. Abreu, M. Bergh, C. Caleman, A. J. Nelson, S. Bajt, J. Chalupsky, H. N. Chapman, R. R. Fäustlin, V. Hajkova, P. A. Heimann, B. Hjörvarsson, L. Juha, D. Klinger, J. Krzywinski, B. Nagler, G. K. Pálsson, W. Singer, M. M. Seibert, R. Sobierajski, S. Toleikis, T. Tschentscher, S. M. Vinko. R. W. Lee, J. Hajdu, N. Tîmneanu
Phys. Rev. E 83, 016403 (2011).

V **Explosion of xenon clusters in ultraintense femtosecond X-ray pulses from the LCLS free electron laser**
H. Thomas, A. Helal, K. Hoffmann, N. Kandadai, J. Keto, J. Andreasson, **B. Iwan**, M. Seibert, N. Timneanu, J. Hajdu, M. Adolph, T. Gorkhover, D. Rupp, S. Schorb, T. Möller, G. Doumy, L. F. DiMauro, M. Hoener, B. Murphy, N. Berrah, M. Messerschmidt, J. Bozek, C. Bostedt, and T. Ditmire
Phys. Rev. Lett. 108, 133401 (2012).

VI **Time of flight mass spectrometry to monitor sample explosion in flash diffraction studies on single virus particles**
J. Andreasson, N. Tîmneanu, **B. Iwan**, M. Hantke, A. Rath, T. Ekeberg, F. R. N. C. Maia, A. Barty, H. N. Chapman, J. Bielecki, C. Abergel, V. Seltzer, J.-M. Claverie, M. Svenda, D. Rolles, L. Foucar, A. Rudenko, R. Hartmann, C. Bostedt, and J. Hajdu
in preparation

Supporting Papers

The author has contributed to the experiments described in the following papers.

VII **Soft X-ray free electron laser micro focus for exploring matter under extreme conditions**
A. J. Nelson, S. Toleikis, H. Chapman, S. Bajt, J. Krzywinski, J. Chalupsky, L. Juha, J. Cihelka, V. Hajkova, L. Vysin, T. Burian, M. Kozlova, R. R. Fäustlin, B. Nagler, S. M. Vinko, T. Whitcher, T. Dzelzainis, O. Renner, K. Saksl, A. R. Khorsand, P. A. Heimann, R. Sobierajski, D. Klinger, M. Jurek, J. Pelka, **B. Iwan**, J. Andreasson, N. Tîmneanu, M. Fajardo, J. S. Wark, D. Riley, T. Tschentscher, J. Hajdu, R. W. Lee
Optics Express 17, 18271 (2009).

VIII **Aerosol imaging with a soft X-Ray free electron laser**
M. J. Bogan, S. Boutet, H. N. Chapman, S. Marchesini, A. Barty, W. H. Benner, U. Rohner, M. Frank, S. P. Hau-Riege, S. Bajt, B. Woods, M. M. Seibert, **B. Iwan**, N. Tîmneanu, J. Hajdu, J. Schulz
Aerosol Sci. Tech. 44, I – VI (2010).

IX **Cryptotomography: Reconstructing 3D Fourier intensities from randomly oriented single-shot diffraction patterns**
N. D. Loh, M. J. Bogan, V. Elser, A. Barty, S. Boutet, S. Bajt, J. Hajdu, T. Ekeberg, F. R. N. C. Maia, J. Schulz, M. M. Seibert, **B. Iwan**, N. Tîmneanu, S. Marchesini, I. Schlichting, R. L. Shoeman, L. Lomb, M. Frank, M. Liang, H. N. Chapman
Phys. Rev. Lett. 104, 225501 (2010).

X **Sacrificial tamper slows down sample explosion in FLASH diffraction experiments**
S. P. Hau-Riege, S. Boutet, A. Barty, S. Bajt, M. J. Bogan, M. Frank, J. Andreasson, **B. Iwan**, M. M. Seibert, J. Hajdu, A. Sakdinawat, J. Schulz, R. Treusch, and H. N. Chapman
Phys. Rev. Lett. 104, 064801 (2010).

XI **Single-shot femtosecond X-ray diffraction from randomly oriented ellipsoidal nanoparticles**
M. J. Bogan, S. Boutet, A. Barty, W. H. Benner, M. Frank, L. Lomb, R. Shoeman, D. Starodub, M. M. Seibert, S. P. Hau-Riege, B. Woods, P. Decorwin-Martin, S. Bajt, J. Schulz, U. Rohner, **B. Iwan**, N. Tîmneanu, S. Marchesini, I. Schlichting, J. Hajdu, H. N. Chapman
Phys. Rev. Spec. Top. 13, 094701 (2010).

XII **Single mimivirus particles intercepted and imaged with an X-ray laser**
M. M. Seibert, T. Ekeberg, F. R. N. C. Maia, M. Svenda, J. Andreasson, O. Jönsson, D. Odic, **B. Iwan**, A. Rocker, D. Westphal, M. Hantke, D. P. DePonte, A. Barty, J. Schulz, L. Gumprecht, N. Coppola, A. Aquila, M. N. Liang, T. A. White, A. Martin, C. Caleman, S. Stern, C. Abergel, V. Seltzer, J. M. Claverie, C. Bostedt, J. D. Bozek, S. Boutet, A. A. Miahnahri, M. Messerschmidt, J. Krzywinski, G. Williams, K. O. Hodgson, M. J. Bogan, C. Y. Hampton, R. G. Sierra, D. Starodub, I. Andersson, S. Bajt, M. Barthelmess, J. C. H. Spence, P. Fromme, U. Weierstall, R. Kirian, M. Hunter, R. B. Doak, S. Marchesini, S. P. Hau-Riege, M. Frank, R. L. Shoeman, L. Lomb, S. W. Epp, R. Hartmann, D. Rolles, A. Rudenko, C. Schmidt, L. Foucar, N. Kimmel, P. Holl, B. Rudek, B. Erk, A. Homke, C. Reich, D. Pietschner, G. Weidenspointner, L. Struder, G. Hauser, H. Gorke, J. Ullrich, I. Schlichting, S. Herrmann, G. Schaller, F. Schopper, H. Soltau, K. U. Kühnel, R. Andritschke, C. D. Schröter, F. Krasniqi, M. Bott, S. Schorb, D. Rupp, M. Adolph, T. Gorkhover, H. Hirsemann, G. Potdevin, H. Graafsma, B. Nilsson, H. N. Chapman, J. Hajdu
Nature 470, 78 (2011).

Reprints were made with permission from the publishers.

Comments on the author's contribution

Paper I: I performed the experiment at FLASH and did the data analysis. I performed simulations on the laser-material interactions and wrote the paper.

Paper II: I participated in the experiment and contributed to the simulations and the writing of the paper.

Paper III: This details the theoretical aspect of Paper IV. I performed plasma simulations, wrote the paper, and presented the results at the conference.

Paper IV: I participated in the experiment at FLASH and contributed to the data analysis with simulations on the experimental setup. I was involved in the writing of the paper.

Paper V: I was involved in the planning of the experiment and participated in the experiment at LCLS. I did additional simulations on the nanoplasma formation and hydrodynamic expansion.

Paper VI: I contributed to the injector design and participated in the experiments at LCLS. I was involved in the data analysis and simulations. I contributed to the writing of the paper.

Contents

Abbreviations

AFM	Atomic Force Microscope
CCD	Charge-coupled Device
CXDI	Coherent X-ray Diffraction Imaging
DESY	Deutsches Elektronen Synchrotron
EUV	Extreme Ultraviolet
FEL	Free-Electron Laser
FLASH	Freie Elektronen Laser in Hamburg
IR	Infrared
LCLS	Linac Coherent Light Source
MCP	Multichannel Plate
MEC	Matter under Extreme Conditions
NLTE	Non–local Thermodynamic Equilibrium
RF	Radio Frequency
SASE	Self Amplified Spontaneous Emission
SEM	Scanning Electron Microscope
SLAC	SLAC National Accelerator Laboratory
TOF	Time of Flight
VUV	Vacuum Ultraviolet
XFEL	X-ray Free-Electron Laser

1. Introduction

The realization that light exists beyond the visible regime set the groundwork for a series of important discoveries and inventions that led to widespread progress in science and technology. The first person to measure the invisible was William Herschel who discovered infrared radiation in 1800 with the help of a simple experiment involving a prism and a thermometer [1]. Almost one hundred years later, in 1895, Wilhelm Röntgen detected X-rays through experiments with cathode-rays in vacuum tubes [2]. He realized that X-rays have a penetration depth that is dependent on the material illuminated and is directly related to the material's ability to absorb. Soon after, his work led to the first X-ray image of a hand.

Although there were initial uncertainties about the nature of these new rays, Röntgen's experiments proved that X-rays can be used to probe matter and image interior structures. A few years later, it was established that these rays are indeed waves of electromagnetic radiation and therefore just another form of light that extends the electromagnetic spectrum towards shorter wavelengths and higher photon energies (Fig. 1.1).

The great potential of this new and energetic radiation became apparent with Max von Laue's discovery of X-ray diffraction by crystals in 1912. X-rays are inherently suitable for producing intense diffraction patterns off crystals since their short wavelengths are usually of the same order of magnitude as the typical distances in a crystal lattice. This discovery revolutionized structural sciences and biology as it created the possibility of studying the atomic structure of biological objects. X-ray crystallography is now one of the most successful methods for the extraction of structural information from biological samples. As of today, over 70,000 structures have been solved with this technique and have been deposited in the Protein Data Bank [3].

The success of X-ray crystallography and further advances in X-ray physics are directly coupled to the quest for brighter and more intense X-ray sources. Synchrotron radiation, now the most common radiation source in X-ray crystallography, started out as a by-product in particle accelerators when it was discovered in 1947 [4]. It took almost 30 more years before its significance for structural biology became apparent. The first dedicated facilities for synchrotron radiation appeared in the late 1970s. They provided very intense and bright X-ray pulses with a peak brightness that surpassed that of common X-ray tubes by a considerable amount. Synchrotron radiation gave a tremendous boost to structural sciences, enabling the study of large and complex systems at improved resolution.

The introduction of wigglers and undulators pushed the performance of synchrotron facilities to much higher levels but there was still a demand for even brighter and shorter X-ray pulses. This demand has been met with recent achievements in the development of X-ray free-electron lasers (XFELs). XFELs produce radiation which exceeds the peak brightness of current synchrotrons by 10 orders of magnitudes. The resulting X-ray pulses possess a high spatial and temporal coherence and can have durations of only a few femtoseconds.

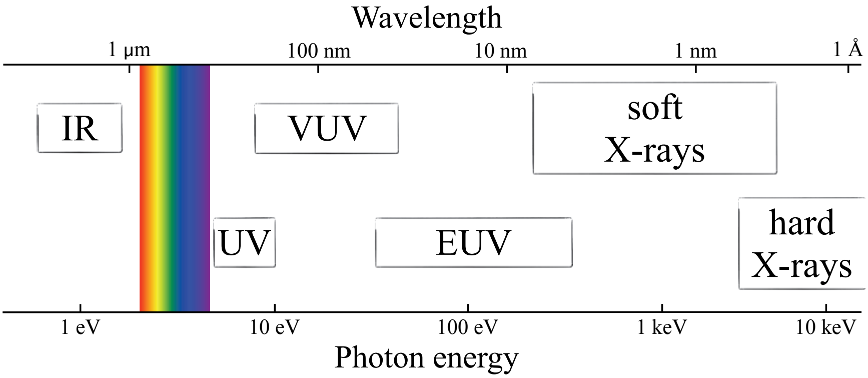

Figure 1.1: Part of the electromagnetic spectrum from the infrared (IR) to the hard X-ray regime. Characteristic wavelengths and photon energies are shown. Visible light ranges from red at 700 nm to violet at 400 nm. Ultraviolet (UV), vacuum ultraviolet (VUV), extreme ultraviolet (EUV), soft X-ray, and hard X-ray radiation are located at shorter wavelengths and higher photon energies.

Diffraction before destruction

Ultrashort and ultraintense laser pulses produced by XFELs are ideal for applications such as probing material properties on an atomic scale and studying the dynamics of different processes in these materials. Short pulses in the soft and hard X-ray regime are also necessary for ultrafast coherent X-ray diffraction imaging (CXDI), a method that records a diffraction pattern of an object before its destruction, and enables the reconstruction of the sample structure from the recorded pattern [5]. Such a diffraction pattern is the result of elastic photon scattering from the object. Elastic scattering is the interaction between photons and electrons without energy transfer and is only one of several potential processes that occur when matter is illuminated with X-rays. Other processes, like photoabsorption and inelastic scattering, deposit energy into the sample, leading to modifications and damage in the material through ionization and heating.

Damage to the sample during exposure poses a problem for obtaining a diffraction pattern that provides enough signal to successfully extract structural information on the illuminated sample. At a wavelength of 1 Å, photoionization accounts for 90% of all photon-material interactions in carbon and is responsible for most of the damage [6]. In conventional X-ray diffraction experiments on crystalline samples, damage is distributed over billions of unit cells in the irradiated volume of the crystal. In addition, periodicity in the crystal structure leads to an enhancement of the scattered signal. X-ray crystallography is in fact an exercise in damage limitation resulting in intense diffraction patterns which enable object reconstructions to high resolution. However, not all samples can be crystallized. Membrane proteins, cells, and large viruses are examples of biological objects that withstand crystallization and would be destroyed if exposed to the amounts of radiation common in X-ray crystallography experiments.

A solution to the damage problem comes from the aforementioned ultrashort and extremely intense laser pulses from FELs and the CXDI method which uses them. Together, they allow for the imaging of biological and other samples that are outside the realm of conventional X-ray crystallography. Here, the incident pulse deposits all its energy directly into the illuminated object and destroys it almost instantaneously but not before an interpretable diffraction pattern is obtained [7]. X-ray pulses have to be short enough to outrun the damage and intense enough to produce an interpretable diffraction pattern before the sample is destroyed [5]. One of the first experiments to prove this concept of *diffraction before destruction* with a biological object was performed at the Linac Coherent Light Source (LCLS) [12], the world's first hard X-ray FEL. In this experiment, mimivirus, one of the largest known viruses that is difficult to crystallize, was successfully imaged [7].

Understanding the processes that govern the interactions when an object is illuminated with an extremely intense and very short FEL pulse is necessary for selecting suitable parameters for ultrafast diffraction imaging experiments. Radiation with energies and wavelengths comparable to characteristic binding energies in different elements and lattice distances in solids can probe electronic or geometric structures with atomic resolution and allows for identification of the chemical composition of complex systems. Pulses with femtosecond duration can potentially be used to take snapshots of material processes or chemical reactions. However, gaining detailed knowledge on the laser-material interaction will not only benefit imaging methods like CXDI. With the development of short wavelength FELs, a previously inaccessible intensity regime becomes available. High intensity radiation of short duration can be used to create and probe extreme states of matter, model astrophysical conditions in the laboratory, or explore the structure of vacuum.

Photon-material interactions at such short wavelengths differ considerably from processes at optical or infrared wavelengths [8]. The availability of X-ray FELs allows for a thorough experimental study of these processes and testing of existing theoretical models. The aim of this thesis is to investigate the different aspects of laser-material interactions at soft and hard X-rays. We performed several experiments using FELs to study the response of different materials to ultrashort and ultraintense laser pulses. The first part of this thesis gives a short description of X-ray sources used in our experiments, illustrates the general setup of such experiments, and explains the dominant processes in the soft and hard X-rays regime (Chapter 2). Chapter 3 describes some of the experimental methods and focuses on the samples exposed to FEL radiation. In addition, it contains a section on the tools used to simulate the interaction processes. Chapter 4 summarizes the results of the data analysis and lists key findings from the experiments. The thesis concludes with an outlook on future possibilities and experiments with FELs.

2. Theoretical considerations

2.1 Free-Electron Laser

Major theoretical and experimental achievements in combining the fields of accelerator physics and laser science led to the development and improvement of a new generation of coherent light sources: Free-electron lasers (FELs). Based on theoretical predictions of coherent light generation from accelerated electron beams [9], the first infrared FEL was built in 1977 [10]. Through the following decades, the wavelength of the emitted radiation was pushed towards shorter values, resulting in the construction of FELs lasing in the optical, VUV, EUV, soft, and hard X-ray regime [11, 12, 13]. FELs in the soft and hard X-ray regime are of special interest as they outperform common synchrotron sources in terms of peak brilliance, photon fluence, and pulse coherence by several orders of magnitudes. The short wavelength and pulses, as well as the high intensities, allow for new and exciting experiments to probe matter under unprecedented conditions or extract structural information from objects before their destruction. As a consequence, new facilities are being built and commissioned all over the world.

The Freie Elektronen Laser in Hamburg (FLASH) was the first FEL built that allowed for user experiments in the soft X-ray regime [11]. General user operation started in 2005 with radiation tunable from EUV (47 nm) to soft X-ray (13 nm)*. The available wavelength has continuously been pushed towards shorter values, and as of 2010, lasing at 4.12 nm has been achieved. The first hard X-ray source was the Linac Coherent Light Source (LCLS) in the United States which started user operation in 2009 [12]. It provides radiation in the range from 2.56 nm to 0.13 nm. Other sources, recently commissioned or under development, include the EUV facility Fermi@Elettra in Italy [15], the hard X-ray facility SACLA in Japan [16], and the upcoming hard X-ray facility European XFEL in Germany [13].

An FEL facility consists of essentially three parts that are needed for light production: a device for electron emission, an electron accelerator, and an undulator. As an example, the setup of the FLASH facility in Germany is shown in Fig. 2.1a. Electrons are created in the electron gun. The emitted electron bunch is small in size and ideally only broadened by space-charge effects in the bunch itself. The quality of the emitted electron bunches is important as it influences the performance of the FEL and the quality of the produced radiation. Several categories of electron guns exist which can be differentiated by the method of electron emission. Both FLASH and LCLS use radio frequency-based (RF) photocathode electron emitters.

Once the electrons exit the gun, they enter the second part of the FEL setup, the linear accelerator (LINAC). Here, the electrons are compressed, accelerated to relativistic energies, and finally collimated before they enter the 3rd stage, the undulator.

---

*FLASH was preceded by the TESLA Test Facility (TTF) which allowed for experiments at wavelengths of $\sim$100 nm and shorter. TTF was renamed to FLASH after a successful proof-of-principle experiment on flash diffractive imaging [14].

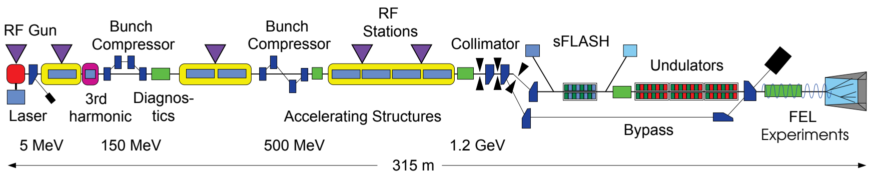

(a) Outline of FLASH, the soft X-ray FEL in Germany

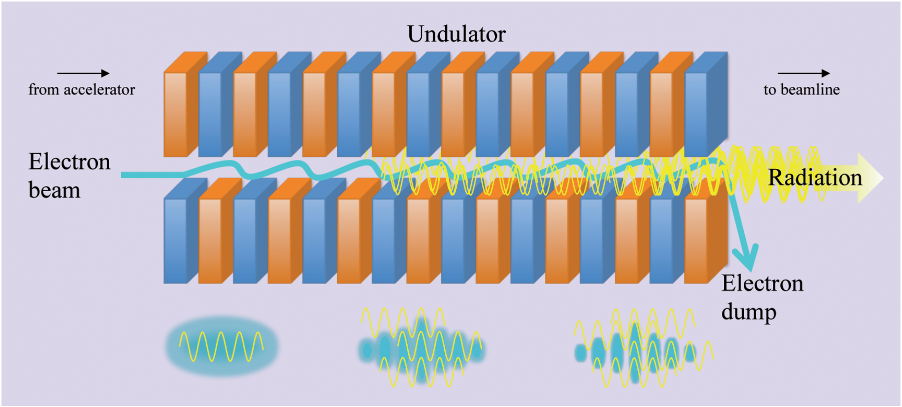

(b) SASE process

Figure 2.1: (a) Schematic outline of FLASH (Hamburg, Germany). Electron bunches are emitted from the RF electron gun. These bunches are accelerated to relativistic energies and start lasing during their travel through the undulator. The electron beam is then dumped and the radiation is transmitted to the different beamlines for user experiments. (Picture taken from [17]) (b) During the SASE process electron density modulations take place until conditions are reached where the electron bunch radiates coherently.

The undulator is a construct of periodically assembled magnets with alternating polarities. The resulting magnetic field forces the electrons onto an oscillating trajectory which in turn initiates the radiation process.

The key feature of FEL radiation is the process of self-amplified spontaneous emission (SASE) which is schematically shown in Fig. 2.1b. Electron bunches, accelerated to relativistic velocities, enter the undulator and start radiating. An entire electron bunch will radiate incoherently during its initial travel through the undulator but small, randomly distributed regions of increased electron density will emit more intense radiation. The occurrence of such statistical fluctuations in the electron density is due to shot noise in the electron gun. If certain conditions are fulfilled, this radiation can interact with the electrons in the bunch as photons and relativistic electrons co-propagate through the undulator. This interaction results in a modulation of the electron density to such an extent that micro-bunching takes place. The electron modulation leads to a further increase of the coherent emission, which in turn enhances the electron-light interaction and creates additional micro-bunching. The process is amplified exponentially until saturation is reached.

The SASE process enforces an electron density modulation that correlates with the wavelength of the emitted radiation. Microbunches are separated by exactly one wavelength. Therefore, radiation from different electrons will add in phase and the total intensity is proportional to N_e^2, with N_e being the number of electrons in the bunch. This proportionality is the same as in the case of one giant particle with N_e charges emitting coherent radiation*. SASE is the process responsible for the positive and unique features of FEL radiation mentioned above: very high spatial coherence, narrow bandwidth, high average and peak brilliance, and average photon numbers per pulse several orders of magnitudes higher than in common synchrotrons [18].

Another unique feature is the ultrashort duration of the resulting laser pulses that, in principle, can be as short as a few hundred attoseconds. The pulse length is essentially determined by the electron bunch duration. As the SASE process is generated from shot-noise in the electron gun, a single pulse consists of several spikes with lengths on the scale of attoseconds.

After it exits the undulator, the electron bunch is dumped using magnetic fields and the radiation proceeds towards the specific user experiments. Inbetween the undulator exit and the experimental endstations, there are monochromators, attenuators, and beam diagnostics that manipulate the beam and measure the beam quality and properties. Information about beam intensity and bandwidth, pulse length, pulse jitter, and pulse energy are used to estimate the experimental conditions at the endstations.

Depending on the experimental requirements, FEL radiation can be further modified. The beam is commonly focused down to μm or sub-μm diameters using appropriate focusing optics and the resulting high intensities are used to probe different materials.

2.2 Experiments

The unique features of FEL radiation allow for a variety of experiments to study atomic processes, examine the modifications initiated by the illumination, extract structural information, or probe matter under extreme conditions.

The work in this thesis is based on several experiments conducted at soft and hard XFEL user facilities in Germany (FLASH) and the USA (LCLS), respectively. In each of these experiments objects are irradiated by very intense and short FEL pulses. We used a variety of materials to study the effect of size, density, and sample composition on the photon-material interaction at different wavelengths and intensities. The samples investigated include molecular clusters from methane and deuterated methane, atomic clusters from xenon, large biological organisms (mimivirus), and metallic solids of niobium and vanadium doped with either hydrogen or deuterium (see Chapter 3.2 for more details). Exposure to the FEL radiation takes place under reduced pressure in a vacuum chamber to minimize the background signal from ionized air (usual working pressures range from 10^{-5} to 10^{-7} mbar).

The experiments can be divided into two categories and schematic views of the setups are shown in Fig. 2.2. In both cases, the FEL beam is focused to a μm or sub-μm diameter and the sample is placed directly into the focus. The main distinction

---

[*] In comparison, the incoherent emission of radiation from an electron bunch with N_e singly charged electrons is proportional to N_e.

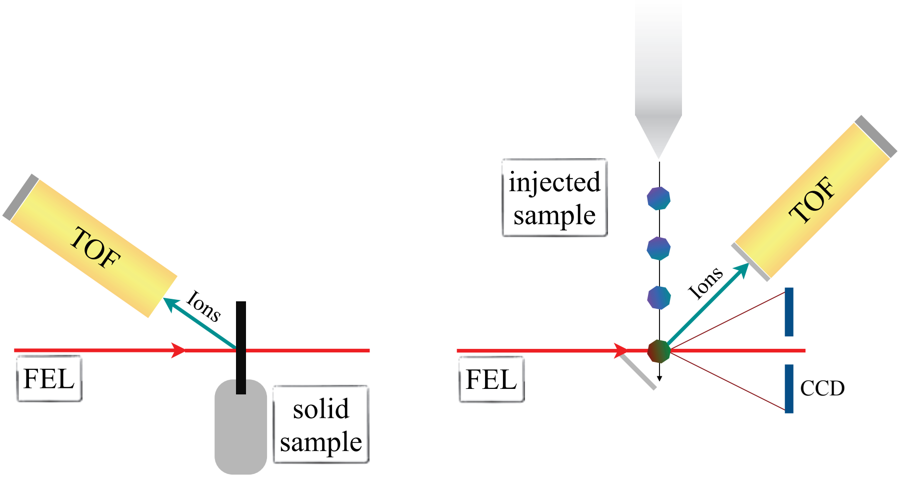

(a) Experiment on solids (b) Injection experiment on clusters and viruses

Figure 2.2: Schematic setup for the different experiments at FELs. (a) Solid metal samples are mounted onto a sample holder and moved into the FEL beam. The TOF spectrometer is operated in drift mode without a repeller or extractor plate. Ions, resulting from the irradiation, can travel freely towards the detector. (b) Clusters and virus particles are injected with either a cluster source or a particle injector. They travel into the interaction region where they are intercepted by the FEL beam. A standard TOF spectrometer with repeller and extractor plate is used in this case and ions are accelerated towards the detector. For additional information, the TOF spectrometer can also be used in drift mode. During experiments on viruses, diffraction patterns are recorded on a CCD camera.

in the setups is in the nature of the samples. Solid samples are placed into a holder that positions them in the focus of the FEL beam. The holder enables controlled sample motions in and out of the beam and ensures that a previously unexposed part of the sample is moved into the beam focus for the next shot. Gaseous samples, simple nanoparticles, and biological samples need to be delivered into the experimental chamber and the interaction region without a container to prevent additional background signal. This is done with the help of various injection devices. In the case of clusters, a cluster source is used to transport gas into the chamber and start the clustering process. For viruses, a particle injector transfers the sample from atmospheric pressure into vacuum.

Information about the induced processes and the sample response to intense radiation is gained through the use of diagnostic tools. An ion time of flight (TOF, see Chapter 3.1) spectrometer is used for data acquisition and is connected to the chamber. It monitors the interaction region and records the signal of ions liberated from an illuminated object. During diffractive imaging experiments, a CCD camera is placed behind the interaction region to record the forward-scattered diffraction pattern from an irradiated object. The pattern itself already reveals size and shape information about the injected sample. Further analysis with help of iterative phase-retrieval and reconstruction algorithms is performed to obtain structural information.

After exposure to FEL pulses, solid samples can be used for further diagnostics on the relevant processes in the materials. Unlike clusters and biological samples, which are completely obliterated by the X-ray irradiation, solids stay mostly intact. The X-ray exposure leads to local damage formation as the sample is generally larger than the focus diameter. The resulting craters, which are due to material ablation on the sample surface, can be studied with either scanning electron microscope (SEM) or atomic force microscope (AFM).

Data analysis is coupled with extensive computer modeling of the interaction dynamics during and after the pulse. Simulations are used to predict the material's response to X-ray illumination and to test the interpretation of the experimental results.

Photon-material interactions include a variety of processes. Therefore, the experimental setup as well as the choice of diagnostic tools has to be tailored towards the information one wants to gain from an experiment.

2.3 Photon-material interactions

X-ray photons can interact with matter in different ways. They can either be absorbed or scattered. Absorption is facilitated primarily in the form of photoionization where photons transfer their entire energy to their main interaction partners, electrons in an atom, and create positively charged ions in the process. Photon scattering is either elastic (coherent scattering) or inelastic (incoherent scattering). Elastic scattering results in momentum transfer and a change of direction for the outgoing photon but no change in kinetic energy. During inelastic scattering, the interaction between photon and electron leads to a transfer of both momentum and kinetic energy.

Absorption and inelastic scattering deposit energy into the material and lead to modifications and structural changes in the illuminated object. Elastic scattering preserves the structural integrity of a sample. All these processes occur simultaneously and can influence the outcome of an experiment in different ways. In diffractive imaging experiments for example, structural information is gained through elastic scattering whereas absorption and inelastic scattering add to the noise. Here, an experimental setup that exploits the information-gaining process and minimizes the effect of the information-altering processes is beneficial.

In **Papers I – V**, an effort is made to gain more knowledge on the interactions and their effect on different materials at short wavelengths. The main focus of **Paper VI** is to understand how these interaction processes influence the outcome of diffractive imaging experiments. Damage and diffraction quality are tightly intertwined and the paper describes the correlation between the two.

2.3.1 Ionization processes

The specific wavelength of a photon defines the way it will interact with a given material. FEL radiation covers a wide range of wavelengths, the focus of this thesis however, lies on the interaction with photons in the soft and hard X-ray regime. At such short wavelengths the material response differs substantially from that at optical or infrared wavelengths (detailed in [19]).

Photon energies, which are inversely proportional to the wavelength according to $E_{ph} = \frac{hc}{\lambda}$, have to be equal to or higher than the ionization potential of electrons in an atom for direct photoionization to occur. Here, photons are absorbed and electrons are ejected with kinetic energies of $E_{kin} = \hbar\omega - E_B$, where $\hbar\omega$ is the photon energy and E_B is the binding energy of the electron. The photon energy also determines which electron will be expelled as the photoionization cross-section is highest when the energy matches or is close to the binding energy of an electron.

In the optical regime, single photons couple mainly to valence or loosely bound electrons. Ionization through photoabsorption is possible in a few materials with ionization potentials low enough for such long wavelength radiation. In the soft and hard X-ray regime, photons are energetic enough to directly target valence and inner-shell electrons. At such short wavelengths, direct photoionization is the primary ionization mechanism (Fig. 2.3a) accounting for $\sim$90 % of all interactions in the case of carbon irradiated with 12 keV X-rays [6].

In the wake of an X-ray photoionization event the atom is left with an electron hole and in an excited state. Depending on the Z number of the atom, two competing relaxation processes occur which start with the transition of an higher-lying electron into the vacancy. For high Z materials atoms can relax mainly through the emission of a fluorescent photon with characteristic energy $\hbar\omega$ that is equal to the difference between the initial and the final atomic state (Fig. 2.3b). In the case of low Z materials the predominant pathway for relaxation is the non-radiative Auger decay (Fig. 2.3c) [20].

The Auger process results in the transfer of energy from the transitioning electron to another electron which is then ejected from the atom. Auger decay is therefore an additional source of ionization at X-ray wavelengths, resulting in a free electron with lower kinetic energy than the primary photoelectron. The kinetic energy of an Auger electron is element specific and corresponds to the difference between the energy of the initial electronic transition and the binding energy of the Auger electron itself [21].

Inner-shell photoelectrons leaving an atom do not only create an electron hole at their former position but can also interact with other electrons on their way out. During this interaction, the departing electron can deposit some of its energy into the atom leading to a state of collective excitation called shake-up. The additional excess energy can be transferred to an Auger electron or it can result in the release of an outer-shell electron in a process called shake-off. The probability for shake-effects is dependent on the chemical environment of the atoms. They contribute to emissions from light elements of biological relevance (nitrogen, carbon, oxygen, and sulfur) [22].

The aforementioned processes are generally referred to as the primary interaction processes when matter is irradiated with X-rays. Depending on the density, size, and composition of the surrounding material, the ejected electrons (photo- and Auger electrons) have a certain probability to interact with other atoms through electron-impact ionization (Fig. 2.3d). Electrons with a kinetic energy E_{i1} can collide with atoms and liberate other electrons in the process. These secondary electrons are usually from an outer-shell. The incident electron imparts some of its energy to the secondary electron to overcome its binding energy and is subsequently scattered off with reduced energy E_{i2}. The secondary electron is ejected from the atom with energy E_s which is typically in the range of a few tens of eV and can participate in further electron collisions which can lead to more impact ionization events. A single photoabsorption event triggers a whole cascade of secondary electrons that will increase the density of free electrons in

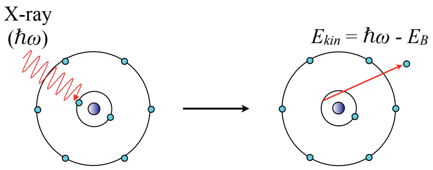

(a) Photoionization

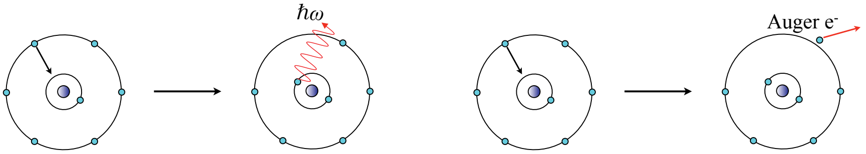

(b) Fluorescent emission

(c) Non-radiative Auger decay

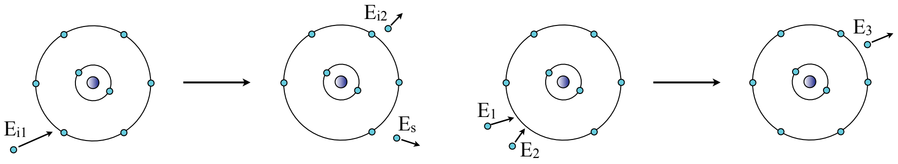

(d) Electron impact ionization

(e) Three-body recombination

Figure 2.3: Photon-atom interaction at X-ray wavelength and resulting processes. (a) Absorption of a photon with energy $\hbar\omega$ and subsequent emission of a inner-shell photoelectron of kinetic energy E_{kin}. A hollow atom is left behind in an excited state. (b) The core vacancy is filled with an electron transitioning from a higher level under emission of a photon of characteristic energy $\hbar\omega$. (c) The vacant core hole is filled through the transition of a higher-level electron into the vacancy. A second electron with characteristic energy is ejected. (d) Photo-, Auger, and secondary electrons with energy E_{i1} participate in electron impact ionization of other atoms in the material, liberating more secondary electrons with lower kinetic energies E_s. The incident electrons travel on with reduced energy E_{i2}. (d) At high enough electron densities three-body recombination can occur when two electrons with energies E_1 and E_2 are simultaneously in the vicinity of an ion. The electron with energy E_1 is captured by the ion and transfers its energy to the second electron which travels on with energy E_3.

the material. The final number of cascade electrons in bulk materials scales with the kinetic energy of the primary electron [23].

At higher electron densities, the inverse of electron-impact ionization can occur, three-body recombination (Fig. 2.3e). When two electrons are simultaneously traveling in the vicinity of an ion, one can be captured in the ion's Coulomb field, whereas the other gains additional energy and escapes into the surrounding system. Specific conditions have to be met for three-body recombination to take place. A high enough electron density and low kinetic energy are necessary for electrons to be able to couple to ions. The decrease in kinetic energy of electrons is achieved through frequent collisions between them which also leads to an equilibration of the electron temperature T_e. On longer timescales, electron-ion equilibration leads to an adjustment of T_e and the ion temperature T_i [21].

The absorption of photons by electrons and the secondary processes it causes leads to strong modifications in the irradiated object. As photoionization is the dominant interaction pathway at X-ray wavelengths ($\sim$90 % for carbon at 12 keV) it accounts for most of the radiation damage in a material. In X-ray diffractive imaging, this is the main reason for a distortion of the diffraction pattern if the X-ray pulses are not short enough to outrun the damage.

2.3.2 Photon scattering

Photon scattering in the form of elastic or inelastic scattering accounts for the other $\sim$10 % of interactions during X-ray irradiation of matter. Elastic scattering, also referred to as Rayleigh or coherent scattering, is a process where a photon scatters off an electron without imparting any energy to it. The photon suffers from a change in direction due to a transfer of momentum. Electrons find themselves in the same electronic states as before the scattering event and the irradiated material sustains no radiation damage. As a consequence, the structural integrity of the material is not altered by this process. Photons interact predominantly with electrons. Therefore, elastic scattering can be used to gain information about the electron density in a material as it probes the electronic structure during the interaction. Approximately 7 % of all interactions in carbon with 12 keV X-rays are elastic scattering events [6]. This makes it the most important process in applications that aim at measuring and determining the atomic structure of an object which relies on locational information about electron densities.

The remaining $\sim$3 % of all X-ray photon interactions is through inelastic scattering (Compton or incoherent scattering). Here, a transfer of energy and momentum occurs between the incident photon and the electron it scatters off. The outgoing photon has thus a different kinetic energy from the incoming one and is deflected in a different direction. Inelastic scattering contributes to the ensuing radiation damage and modifications in the material. In imaging experiments, it contributes to noise in the diffraction pattern. In experiments dedicated to measuring the scattered photon spectra, it is a valuable source of information on a material's electronic setup and important plasma properties [5, 21].

2.3.3 High intensities

The ionization and scattering processes presented in Sections 2.3.1 and 2.3.2 can generally be described within a perturbative framework. The material response to X-ray intensities is treated linearly. The linear and pertubative description of photon-material interactions is expected to break down at very high intensities when nonlinear effects can occur. This is well known in the optical regime where nonlinear phenomena, such as multiphoton absorption, over-the-barrier and tunneling ionization, are responsible for strong ionization effects in materials [19]. Photon energies in the long wavelength regime are not energetic enough for direct single photon ionization. Therefore, high intensity driven ionization is dominant. In the X-ray regime, a single photon can have enough energy to liberate an electron and ionize an atom. For short wavelengths, single photon ionization is the dominant process over a wide range of intensities [6].

Nonlinear effects become relevant at laser intensities and corresponding electric field strengths that compete with the Coulomb binding field strength, $E_C = 5.14 \times 10^9$ V/cm [19, 21]. The relationship between electric field strength E and laser intensity I is expressed through

$$I = \frac{1}{2} c \varepsilon_0 E^2 , \tag{2.1}$$

where c is the speed of light and ε_0 is the permittivity of free space. The intensity corresponding to the Coulomb binding field strength calculates as $I_C \approx 3.51 \times 10^{16}$ W/cm^2. FLASH and LCLS already provide pulses with such intensities, however, another factor influences the occurrence of nonlinear effects, the ponderomotive potential or quiver energy

$$U_P = \frac{e^2 E^2}{4 m_e \omega^2} , \tag{2.2}$$

where e is the electric charge, E is the electric field strength of the incoming radiation, m_e the electron mass, and ω the frequency [21].

When electrons are exposed to the electromagnetic field created by the incident radiation, the field can force an oscillatory motion onto the electrons. They will start to quiver in response to the field with an amplitude that is proportional to $\frac{E}{\omega^2}$. At X-ray wavelengths, the ponderomotive energy is several orders of magnitude smaller than in the optical regime [21].

Nonlinear ionization processes can be separated into two regimes, where either multiphoton or field ionization dominates. The defining parameter that makes a distinction possible is the Keldysh parameter:

$$\gamma = \sqrt{\frac{I_p}{2U_p}} , \tag{2.3}$$

where I_P is the ionization potential and U_P the ponderomotive energy.

For $\gamma \gg 1$, multiphoton ionization is the dominant ionization pathway in the optical regime (Fig. 2.4a). It takes place as either simultaneous or sequential absorption of multiple photons. In the X-ray regime, single photon ionization is the dominant process with cross-sections that are significantly higher than for multiphoton events. A single X-ray photon is usually sufficient to lift an electron into the continuum. For

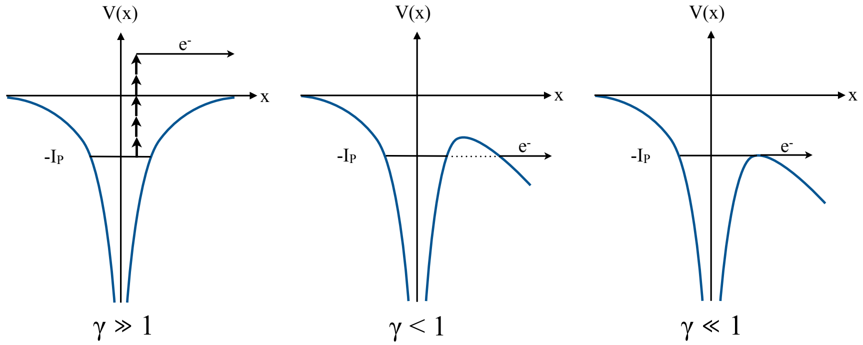

(a) Multiphoton ionization (b) Tunneling ionization (c) Over-the-barrier ionization

Figure 2.4: Schematic illustration of nonlinear multiphoton and field ionization processes during exposure to intense radiation. (a) Multiphoton ionization is considered to be dominant for $\gamma \gg 1$. Ionizing photons are depicted as arrows. (b, c) Field ionization processes like tunneling and over-the-barrier ionization, dominate for $\gamma < 1$ and $\gamma \ll 1$.

this reason, multiphoton events will occur mainly in form of sequential photoabsorption. Here, several single photoabsorption events in one atom happen on a timescale that is shorter than the one needed for relaxation processes. Simultaneous multiphoton ionization can also take place, albeit with a low probability. Simultaneous absorption of multiple photons manifests itself as above-threshold ionization where an electron absorbs more photons than are necessary to overcome its binding energy [21].

For $\gamma < 1$, field ionization, in the form of tunneling or over-the-barrier ionization, dominates. The electric field strength of the laser is high enough to distort the atomic potential, forming a barrier through which an electron can tunnel (Fig. 2.4b). At even higher field strengths ($\gamma \ll 1$), the barrier is further lowered to the point where tunneling is no longer necessary and the electron is unbound (Fig. 2.4c).

The important experimental and beam related parameters for experiments described in **Paper I – VI** are summarized in Table 2.1. Wavelength λ, pulse intensity I, electric field strength E, ponderomotive energies U_P, and the associated Keldysh parameter γ for the case of a singly ionized hydrogen atom are used to define the

λ (nm)	d_{Focus} (μm)	t_{Pulse} (fs)	I_{Peak} (W/cm^2)	E (V/cm)	U_P (eV)	γ	Paper
13.5	20	15	5×10^{14}	6.14×10^{8}	8.5×10^{-3}	28.3	I
13.5	0.8	15	3×10^{17}	1.50×10^{10}	5.07	1.2	II – IV
1.46	1.6	150	6×10^{16}	6.72×10^{9}	0.01	26	V
0.6	3	40	5×10^{17}	1.94×10^{10}	0.02	18.4	VI

Table 2.1: Beam related parameters for the experiments described in this thesis. Wavelength λ, beam diameter d_{Focus} in best focus, and pulse length t_{Pulse} are used to calculate the peak pulse intensity I_{Peak}, electric field strength E, the ponderomotive energy U_P, and the Keldysh parameter γ. The experiments in Paper I – IV were conducted at FLASH, the ones in Paper V and VI at LCLS.

dominant ionization regime. There is a significant spread in the values due to different experimental conditions. At the time of writing this thesis, these are the highest intensity studies performed with X-rays. As the Keldysh parameter indicates, the high-field regime has not yet been reached but conditions in **Paper IV** were getting close to it.

2.4 Definition of plasma

The processes described in Section 2.3 are responsible for the fact that any material irradiated with an intense laser pulse will eventually turn into a plasma. Photoionization of atoms and the resulting secondary electron cascades increase the density of ions and unbound electrons in the material. The sample is heated to a high temperature (several eV to hundreds of eV) in the process.

An equilibrium plasma is an assortment of charged and neutral particles that is considered to be quasineutral and in which all particles display collective behavior. The quasineutrality is expressed in the ability of a plasma to shield electric potentials. This screening of charges, called Debye shielding, acts over a certain length scale which is generally referred to as the Debye length λ_D of a plasma. The Debye length is the radius of a sphere that screens locally arising charges and is defined as

$$\lambda_D = \sqrt{\frac{\varepsilon_0 k_B T_e}{n_e e^2}} \,, \tag{2.4}$$

where ε_0 is the permittivity of free space, k_B the Boltzmann constant, T_e the electron temperature, n_e the electron density and e the electron charge. When the system length over which a plasma is observed is much larger than the Debye length ($L \gg \lambda_D$), the plasma is considered to be neutral. The approximation is then valid that electron and ion densities are almost equal ($n_e \cong n_i = n$) [24].

The Debye length is also used for the definition of the so-called plasma parameter

$$\Lambda = 4\pi n \lambda_D^3 \,, \tag{2.5}$$

which is a measure for the number of particles in a Debye sphere. For a plasma to exhibit collective behavior, $\Lambda \gg 1$ has to be fulfilled. This describes a densely populated Debye sphere which is characteristic for a weakly coupled plasma.

Weakly coupled plasmas are diffuse and hot. Collisions between charged particles occur but they dampen the overall plasma oscillations only to a small extend. Generally, the collision frequency ν between particles is much smaller than the plasma frequency ω_P which ensures collective behavior throughout the plasma. The plasma frequency is defined as

$$\omega_P = \sqrt{\frac{e^2 n_e}{m \varepsilon_0}} \,, \tag{2.6}$$

where e is the electric charge, n_e the number density of electrons, m the electron mass, and ε_0 the permittivity of free space. This is the frequency of collective oscillations of free electrons in the plasma [21, 24].

Quasineutrality and collective behavior are key parameters for the state of an object to be defined as an equilibrium plasma. Both can be observed on system lengths much larger than the Debye length and during observation times longer than a plasma period $\tau_P = \frac{1}{\omega_P}$. The three plasma parameters, ω_P, λ_D, and Λ, are ideal to judge the validity of quasineutrality and collective behavior in a plasma.

The theoretical formalism that governs plasma dynamics depends on the application and what information one wants to gain. Commonly, a classical description is adequate as plasmas exhibit fluid-like as well as particle-like traits. A kinetic approach is utilized when knowledge of the velocity distribution of a system of charged particles is important. In the case of weakly coupled plasma the velocity distribution has to satisfy the Vlasov equation, a simplified form of the Boltzmann equation. This can be expanded to incorporate binary collisions by using the Fokker-Planck equation [21]. When velocity distributions are of no concern, fluid theory provides a sufficient description of a plasma. The necessary equations that govern the plasma behavior in this approach are the fluid equation of motion, the equation of continuity, and the equation of state. These equations can be derived from the Boltzmann equation [24].

Under local thermodynamic equilibrium (LTE) conditions, the ionic and atomic populations in a plasma are calculated using the Saha-Boltzmann equation which follows the fractional ionization for specific gas temperature and electron-ion densities. The gas temperature is taken to be equivalent to the electron temperature. With the photon energies, pulse intensities, and pulse durations used during the experiments described in the papers of this thesis, the assumption of LTE does not hold anymore. During the exposure to ultrashort and ultraintense radiation, conditions are reached in the target that are far from thermal equilibrium. Plasmas are now non-equilibrium plasmas and have to be treated as non–local thermodynamic equilibrium (NLTE) systems in which atomic populations and transitions are followed in detail (see Section 3.3.2).

2.5 Ion acceleration and plasma expansion

When the exposure to intense X-ray radiation turns a sample into a plasma, the temporal evolution of that plasma depends strongly on a series of initial conditions. The density and size of the irradiated material and the intensity of the incident X-ray pulses influence the formation and development of the plasma. Throughout the work contained in this thesis a variety of materials were used to cover a wide range of attributes and study the material response and the dynamics of plasma formation. The different samples are described in detail in Section 3.2.

These materials can generally be separated into two classes for a simplified description of the plasma evolution. Based on their size, the samples can be described as either sphere-like objects in the gas phase or bulk solids. Clusters and viruses were used in the experiments in **Paper I**, **V**, and **VI**, and belong to the first class, with diameters ranging from 2 nm to 500 nm. They are smaller than the incident FEL beam diameters and the attenuation lengths of the X-ray pulses used in the experiments. Therefore, we can assume uniform illumination and ionization of these samples. Bulk metal solids, used in **Paper II** – **IV**, fall into the second category. They have a higher density[*]

---

[*] The densities for the different materials are:

Clusters: $\rho_{CH_4} = 0.422$ g/cm^3, $\rho_{Xe} = 3.057$ g/cm^3
Virus: $\rho_{mimi} = 1.0$ g/cm^3
Metals: $\rho_V = 6.0$ g/cm^3, $\rho_{Nb} = 8.57$ g/cm^3

and are much larger than the other samples, with dimensions that exceed the incident beam diameter and attenuation length ($12 \times 12 \times 1$ mm^3 and $10 \times 10 \times 3$ mm^3). The exposure is hence limited to only a small part of the sample due to their size.

Coulomb explosion

In small targets, photo- and Auger electrons have a sample-size dependent probability to escape their surroundings and leave behind a positively charged sample. The size of the sample determines the amount of positive charges that can accumulate. If the sample is small enough, the number of positive charges will be small, and photoelectrons have a higher probability to overcome the growing positive potential and escape. As the positive charge grows, the ensuing electrostatic repulsion forces the object to undergo a rapid and violent explosion that completely obliterates the sample and accelerates ions to high kinetic energies (Fig. 2.5). This explosion is generally referred to as Coulomb explosion.

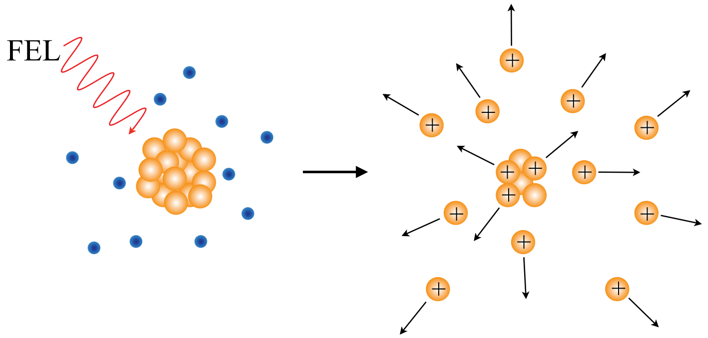

Figure 2.5: Coulomb explosion of a small cluster after exposure to an X-ray pulse. The incident radiation ionizes the sample and liberates photoelectrons (blue). Due to the small sample-size the amount of positively charged ions is limited and photoelectrons are able to leave. The resulting charge build-up leads to electrostatic repulsion between the positive ions and the sample expands in a rapid Coulomb explosion.

Hydrodynamic expansion

In larger objects the target response is more elaborate. Photoionization liberates electrons that cause additional ionization through secondary electron cascades. This results in a rapid build up of positive charge in the sample which effectively prevents the photoelectrons from escaping. Trapped electrons then move inwards to neutralize those positive charges, forming a quasineutral plasma core. Amplified electron and ion motion within the sample leads to an increase in pressure and temperature which is responsible for a hydrodynamic expansion of the entire object.

Electrostatic Coulomb repulsion is still prevalent even in bigger objects but this effect is limited to the surface of the sample. Electrons that leave the sample during the pulse and those that move inward to neutralize the positive charge build-up, leave behind a positively charged surface layer that burns off. Ions originating from the sample surface are accelerated to high kinetic energies whereas ions from the core will expand more homogeneously and gain lower energies.

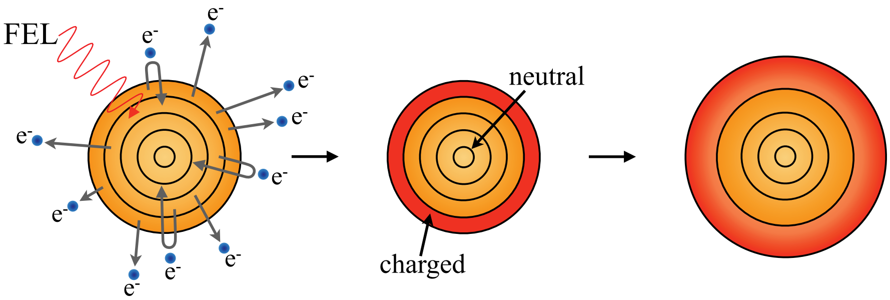

Figure 2.6: Hydrodynamic expansion of a sample after exposure to an X-ray pulse. The incident radiation ionizes the sample and liberates photoelectrons (blue). Initially, some of the electrons can escape, resulting in a build-up of positive charges in the sample. At some point during the charging, the positive potential becomes too strong and electrons are trapped. The sample develops a charged outer layer and a neutral core. Coulomb effects and pressure lead to an expansion of the sample.

Sample size is only one of the factors that influence the target response to X-ray illumination. Other factors are the energy and the intensity of the incident radiation. Pulses with high intensities are more efficient in ionizing the sample than low intensity ones[*] and highly energetic photons create photoelectrons with high kinetic energies. Thus, samples reach a higher average ionization during the pulse when irradiated with high intensity pulses and energetic photoelectrons have a higher probability to escape. The result is a fast charging of the sample which can push the boundary between Coulomb explosion and hydrodynamic expansion towards bigger sizes and leads to an improved acceleration of ions to higher kinetic energies. The size- and intensity-dependency of the expansion dynamics in molecular clusters has been investigated in **Paper I**. The formation of nanoplasma and subsequent hydrodynamic expansion of rare gas clusters is the topic of **Paper V**.

Solids in very intense X-ray beams

The picture changes when turning towards bulk solid materials. As the FEL beam is focused down to a few μm in diameter the sample exposure is locally confined and the illumination with very short and highly intense FEL pulses leads to the formation of defined craters. These are areas on the sample surface where material is removed in a process called ablation. When the laser fluence is comparable to the ablation threshold of the irradiated object, the laser is able to initiate surface ablation and shallow imprints of the laser profile are visible. At higher fluences, a single pulse can heat up more material deeper in the object. Thus, more material is removed and craters are formed. Damage formation, melting, and ablation have been studied extensively in the visible regime [27, 28]. However, at X-ray wavelengths, it is still an active area of research and more experiments and theoretical modeling are needed to completely understand the mechanics.

---

[*] At very high intensities and short pulses, the ionization process saturates as the available electrons are depleted and relaxation processes have not yet refilled the electron holes [25, 26].

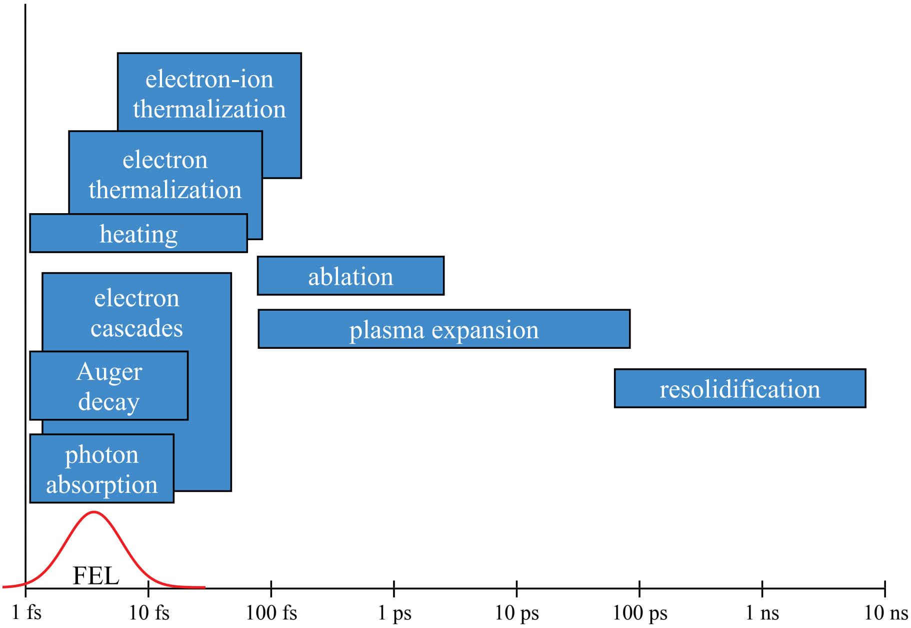

Figure 2.7: Schematics for the timescales of various processes initiated by the irradiation of a bulk solid material with an XFEL pulse.

Damage formation and ablation mechanisms in solids are strongly dependent on the wavelength and intensity of the incident pulses. In **Paper IV** we propose a model to describe the temporal evolution of solid density plasmas in metal samples and explain the responsible factors for material ablation and crater formation.

Fig. 2.7 shows the different processes and approximate timescales in a bulk solid illuminated by a $\sim$10 fs long XFEL pulse with an intensity in the range of $\sim 5 \times 10^{16}$ W/cm^2 which is comparable to that in **Paper IV**. Such pulses have a fluence that is well above the melting and ablation thresholds of the irradiated material and the exposure results in the formation of a plasma and significant damage in the sample surface.

During the pulse, energy is deposited into the sample through *photon absorption*, followed by *Auger decay* and *electron cascades*, which leads to an increase in average ionization, temperature, and pressure in the material. This *heating* is facilitated by *electron thermalization* and *electron-ion thermalization* and triggers a fast transition from solid bulk matter to hot and dense plasma with temperatures of up to 400 eV. The incident X-rays can induce a surface transparency due to saturation of the ionization [25] and thus reach greater depths in the sample. As the pulse travels deeper into the material the fluence will decrease to a value that is similar to the ablation threshold of the irradiated sample. At this point, the liberation of electrons into the lattice decreases to the level of a critical electron density of $N_e \approx 10^{22}$ cm^{-3}. This density sets a lower limit for the number of free charge carriers necessary to destabilize the lattice of solid materials due to ultrafast, nonthermal melting and can be used to predict a

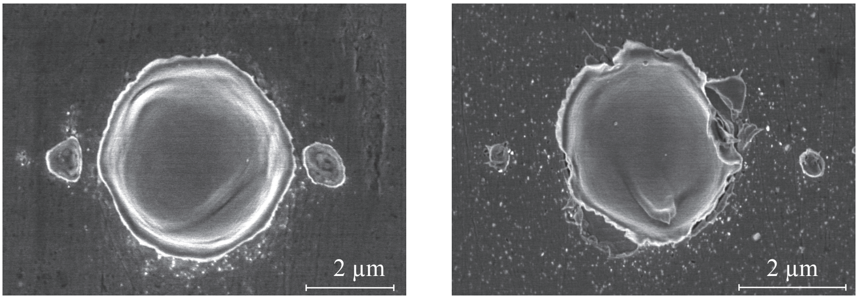

(a) Nb crater (b) NbD crater

Figure 2.8: SEM images of ablation craters in solid metals. The samples have been irradiated with 15 fs long soft X-ray pulses at $\lambda = 6.8$ nm with intensities in the range of 10^{16} W/cm^2. (a) Single crystal niobium (Nb). The two small craters left and right of the main crater result from additional lobes in the FEL beam profile. (b) Ablation crater in deuterated polycrystalline niobium (NbD).

critical depth for initial crater formation. At densities exceeding the critical density, a homogeneous transformation from solid to liquid state is possible in a short time. Nonthermal melting and subsequent *ablation* occur on much shorter timescales (a few hundred femtoseconds) than conventional thermal melting processes which act on picosecond timescales [29]. Crater formation to greater depths than the critical depth is most likely due to these conventional thermal melting processes and hydrodynamic *plasma expansion* on timescales longer than 1 ps. Finally, on nanosecond timescales, after the sample cools down due to expansion and removal of molten material, *resolidification* sets in and the craters take on their final forms. Fig. 2.8 shows SEM images of ablation craters in solid metals, single crystal niobium (Nb) and deuterated polycrystalline niobium (NbD). These craters result from the exposure of the sample surface to intense and short soft X-ray pulses at $\lambda = 6.8$ nm. These pulses reached intensities of more than 10^{17} W/cm^2.

Ion acceleration is connected to the expulsion of material from the illuminated area. During the pulse and shortly after it, when plasma forms, very hot and energetic ions located close to the surface are ejected from the sample. This ion front can be modeled with a self-similar isothermal fluid model which shows good agreement with our experimental data [30]. This model has been used to describe proton acceleration from solids irradiated with high-intensity lasers at various wavelengths [31].

3. Methods and data analysis

In the first set of experiments described in **Paper II** – **IV**, a solid object is illuminated by intense FEL pulses. A simplified illustration of the experimental setup can be seen in Fig. 2.2a. In the second set of experiments (**Paper I**, **V**, and **VI**), depicted in Fig. 2.2b, aerosolized samples are delivered into the interaction region and intercepted by the FEL pulses "on the fly". The different setups are necessary to accommodate the different nature of the samples. Solid bulk samples have to be mounted in the experimental chamber, whereas small, low density samples, like clusters and viruses, can be injected. It is possible to deposit some of the low density samples onto a substrate material and mount them in the chamber, an approach that was included in earlier experiments on biological cells [32]. However, injection is preferred as it allows for a substrate-free illumination of an isolated sample, which reduces background.

In both setups, a time of flight (TOF) mass spectrometer can be used for data acquisition. The data analysis on the resulting mass spectra is combined with extensive computational modeling, which allows for a comparison of the experimental results with theoretical models.

The following sections will give a detailed overview on the principles of TOF measurements, the samples used in the experiments, and the computational tools employed to simulate and analyze the outcome of photon-material processes in a sample.

3.1 Time of flight measurements

Most of the TOF data described in this thesis were recorded with a linear ion-TOF spectrometer. Illumination with an intense X-ray pulse releases electrons from the sample, leaving behind a rich variety of positive ions. The charge and kinetic energies of these ions give information about the explosion process and the fragmentation of the sample.

The principle of mass separation of ions has been discovered by J. J. Thompson [33]. Over the years, this method has been refined to create a powerful tool to probe the structure and composition of different substances. An important attribute of TOF measurements is the ability to examine the interaction of ionizing radiation with atoms and electrons in a material through the detection of the interaction products.

A general setup of a TOF spectrometer is shown in Fig. 3.1a. The basic idea behind such a setup is the measurement of arrival times of ions. These measurements can be performed in two different ways, active or drift mode. In active mode, the ion source is located in the interaction region between two charged plates, generally referred to as the repeller and extractor plate. The source can be any sample exposed to radiation energetic enough to achieve ionization. The plate voltages V_1 and V_2 generate an electric field that accelerates the resulting ions towards a field-free drift tube. The ions travel through the drift region and are recorded on a detector located at the end

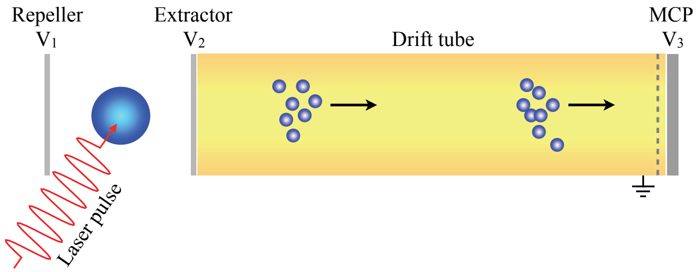

(a) TOF for active or drift mode measurements

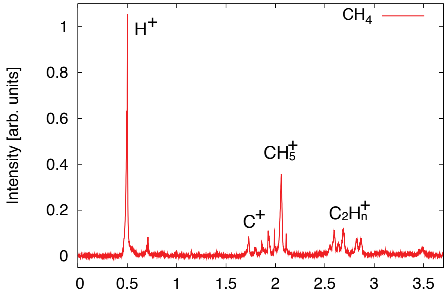

(b) Spectrum from a methane cluster

Figure 3.1: General setup for TOF measurements. (a) The interaction region is located between the repeller and extractor plate, which can each be held at a constant voltage (V_1, V_2) to create an electric field in this region. Positive ions can be accelerated towards the field-free drift tube. Depending on their mass-to-charge ratio, they travel at constant velocity and are detected upon impact by a MCP detector held at voltage V_3. The ion signal is recorded as a function of arrival time. In drift mode, the repeller and extractor plates are omitted. The ions travel without interference towards the MCP. A high-pass filter in front of the detector (dotted line) can be used to select a specific energy range of ions. (b) TOF spectrum of a methane cluster irradiated by soft X-ray pulses at 13.5 nm wavelength and pulse intensity of 5×10^{14} W/cm^2.

of the tube. Usually, a multi-channel plate (MCP) detector is used that records the ion signal and arrival time upon impact. The data are then visualized in form of TOF spectra (Fig. 3.1b) with peaks at specific times corresponding to ions of a certain mass and charge state. Variations in the initial ion energy, position, formation time and formation mechanism will result in a spread in the arrival time distribution and affect shape and width of the peaks. In an accelerating field, the velocity v of such ions is proportional to

$$v \propto \sqrt{\frac{q}{m}}\,, \tag{3.1}$$

where q is the charge state of the ion and m its mass. As a result, the ion time of flight is uniquely related to the square root of the mass-over-charge (m/q) ratio [34].

Scattered photons from the sample can also be detected and result in a sharp peak in the TOF spectrum. The time difference between the photon peak (considered as t = 0) and the different ion peaks can be used to determine m/q ratios.

In drift mode, the repeller and extractor plate in Fig. 3.1a can be omitted. Contrary to the active mode, where ions are separated by mass and charge, no active separation is performed. Particles leave the interaction region in all possible directions but only the fraction that initially moves towards the MCP will be detected. Very fast particles will be detected first, slow ones will be detected last. If the difference between the flight times of specific species is sufficiently high, single peaks may be visible. At small differences, the flight spectrum displays a continuous distribution.

Drift measurements are useful if one is interested in a direct projection of the interaction region in terms of kinetic energies. As there are no accelerating fields, ion energies are unaltered and the arrival time of ions is directly correlated to their initial kinetic energy.

Thin metallic grids can be mounted in front of the MCP. If voltage is applied to them, they can act as high-pass filters that allow for a pre-selection of ion energies. The voltage defines a lower limit for the kinetic energies and only ions with an energy above this limit are able to pass and be detected. Scanning a series of different voltages allows for a better determination of the ion kinetic energy range in an experiment. Fig. 3.2 shows the effect of different grid voltages on a TOF spectra.

Spectra from active mode, as well as drift mode measurements, can be used to identify different material fragments and deduce the kinetic energy of ions.

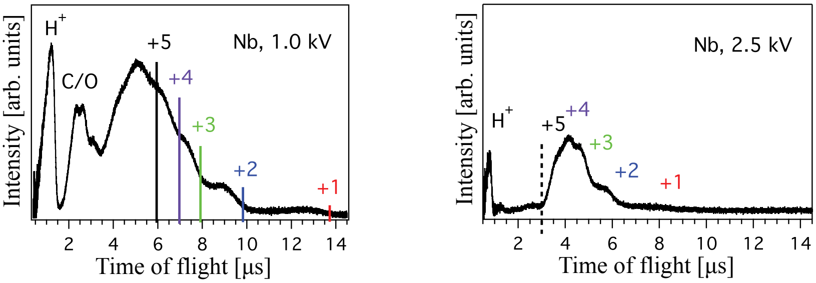

(a) High-pass filter of 1 kV

(b) High-pass filter of 2.5 kV

Figure 3.2: Averaged ion TOF spectra from drift measurements on solid niobium metal irradiated with 15 fs long soft X-ray pulses at $\lambda = 13.5$ nm and pulse intensity of 10^{17} W/cm^2. Not all peaks are resolved. (a) A voltage of 1 kV is applied to the high-pass filter grids and results in cut-offs for different charge states (vertical lines). (b) A grid voltage of 2.5 kV results in the suppression of low energetic peaks (C, O). High energetic ions shift to shorter flight times and reveal a different distribution than in (a).

3.2 Samples

3.2.1 Clusters

Clusters were discovered in 1956 [35], and represent a transition between atomic or molecular gases and bulk material. They are generally defined as aggregates of atoms or molecules with numbers ranging between 2 and 10^7. Clusters that are build from identical atoms are referred to as homo-nuclear clusters. In the case of differing constituent atoms they are called hetero-nuclear clusters.

Clusters are formed when gas is supersonically expanded through a conical nozzle into an environment at very low pressure. The expansion is adiabatic, accompanied by many collisions between the gas particles, resulting in an efficient cooling of the gas vapor. As the gas cools, it enters a supersaturated state and the collisions between particles lead to the formation of dimers which act as nucleation sites for clusters. Further condensation onto these nucleation sites increases the size of these complexes. Additional cooling is achieved through evaporation of particles off the cluster surface. The formed complex is held together by interatomic and intermolecular bonding and interaction forces. Among them, van der Waals and London dispersion forces, dipole-dipole interactions, and hydrogen bonds [36, 37].

The method described above is one of the standard techniques for cluster creation and has been used in the experiments of **Paper I** and **V**. Figs. 3.3a–c show illustrations of such clusters made from methane and xenon gas.

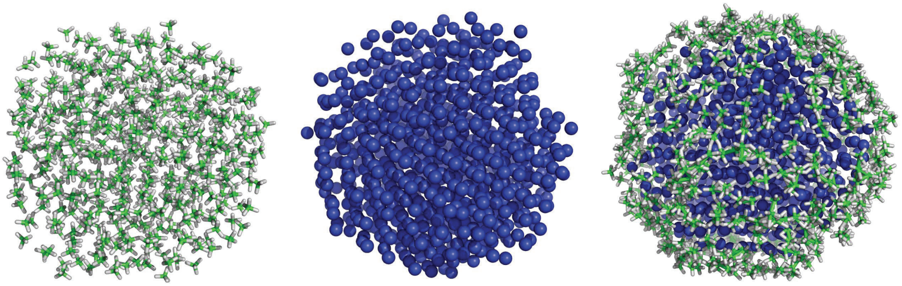

(a) Methane cluster (b) Xenon cluster (c) Doped cluster

Figure 3.3: Illustration of various clusters simulated with the molecular dynamics software GROMACS [38]. (a) Molecular methane cluster containing carbon (green) and hydrogen (white) atoms. (b) Rare gas cluster from xenon. (c) Methane cluster doped with xenon atoms (blue).

The size of a cluster depends on several experimental parameters that can be tuned. Backing pressure p_0 and temperature T_0 of the gas in the cluster source as well as the nozzle geometry influence cluster formation. Generally, after choosing a suitable nozzle, increasing p_0 or decreasing T_0 increases cluster size. Under fixed conditions (constant p_0 and T_0), clusters follow a log-normal size-distribution. The mean size $\langle N \rangle$ can be derived from the empirical Hagena scaling law [39],

$$\Gamma^* = \frac{k \cdot p_0}{T_0^{2.2875}} \left(\frac{d}{\tan \alpha} \right)^{0.85} . \tag{3.2}$$

The Hagena parameter Γ^* is a function of the experimental parameters, p_0 and T_0. The nozzle geometry is accounted for by d, the nozzle diameter, and α, its opening half-angle. The coefficient k is a constant describing the intermolecular bonding potential of the gas and is related to the sublimation energy and bulk density of the material [40]. The Hagena parameter is used to calculate the mean cluster size $\langle N \rangle$:

$$\langle N \rangle = \begin{cases} 38.4 \cdot (\frac{\Gamma^*}{1000})^{1.64} & 350 < \Gamma^* < 1800 \,, \\ 33 \cdot (\frac{\Gamma^*}{1000})^{2.35} & 1800 < \Gamma^* \,. \end{cases} \tag{3.3}$$

Doped clusters

Doped clusters contain two or more different types of constituents. Using a pick-up technique, the surface of a cluster can be doped with atoms or molecules from another gas. Here, clusters are produced as described above but the cluster beam crosses another low pressure gas beam containing a dopant. Gas particles can now condense on the cluster surface. Increasing the pressure in the doping gas leads to enhanced condensation and to the formation of heavily doped clusters. Furthermore, it is possible for particles from the doping gas to form small clusters in and on the original cluster. As a consequence, the additional heat from the cluster formation results in the evaporation of the original cluster constituents, leaving behind a new cluster made entirely from the doping gas [41].

Clusters can be created from the majority of elements in the periodic table. Metallic, molecular, or rare gas clusters show a rich variety of unusual physical properties [37].

Paper I describes experiments on molecular clusters of pure and heavy methane (CH_4, CD_4) at FLASH. Both CH_4 and CD_4 are expected to yield similar cluster size distributions under the same experimental conditions. At a fixed gas temperature of $T_0 = 160$ K and gas backing pressures p_0 between 1.8 bar and 18 bar, clusters containing 1×10^3 – 2.5×10^5 molecules were created. This corresponds to cluster radii between 2.46 nm and 15.5 nm. The clusters were illuminated with 15 fs soft X-ray pulses at a wavelength of 13.5 nm and pulse intensities ranging from 10^{13} W/cm^2 to 10^{15} W/cm^2.

Rare gas clusters of xenon were the target in experiments at LCLS described in **Paper V**. Xenon gas was expanded through a conical nozzle of 100 μm diameter at a backing pressure of $p_0 = 8.2$ bar and $T_0 = 300$ K. At such conditions, clusters with an average size of 10,000 atoms were produced ($\sim$5.5 nm radius). They were irradiated with 150 fs long X-ray pulses at $\lambda = 1.46$ nm and pulse intensities between 4×10^{14} W/cm^2 and 6×10^{16} W/cm^2.

3.2.2 Biosamples

Single virus particles and small living cells represent a transition between heteronuclear clusters and bulk biomaterials. Blurring the line between cellular life and viral structures, mimivirus (*Acanthamoeba polyphaga Mimivirus*) is one of the largest known viruses [42]. It is a member of the family of Mimiviridae. Mimivirus is visible in a light microscope and its size is comparable to that of a small cell. This has been the cause for its initial misidentification as a microbe. Its name, mimivirus, reflects this mistake and stands for "microbe-mimicking virus". Analysis of the genome sequence reveals it to be a virus with more genes than many parasitic bacteria and with additional cell-like genes previously not found in viruses [43]. Another trait, formerly only attributed to cells, is the ability to be infected with a virus. It has been shown that small viruses, so-called virophages, can infect mimivirus and use its replication machinery to express their own genes [44].

Mimivirus (Fig. 3.4) consists of a pseudo-icosahedral viral capsid with a diameter of 0.45 μm which is covered entirely in fine hairlike fibers, extending its diameter to a total of 0.75 μm [43, 45]. Its size and the outer layer of fibers pose problems in determining the interior structure of the capsid. As of yet, a successful three-dimensional reconstruction from cryo-electron microscopy images has not been possible. A conventional crystallographic approach is hindered by the inability to crystallize the virus.

All these factors make mimivirus a prime target for single-shot diffraction imaging experiments with ultrashort and ultraintense FEL pulses. In a proof-of-principle experiment for CXDI of biological objects [7], mimivirus particles were injected into the focused beam of the LCLS. Illumination with 70 fs long pulses at $\lambda = 0.69$ nm and with peak intensities of 6.5×10^{15} W/cm^2 resulted in diffraction patterns that were successfully reconstructed to a resolution of 32 nm. The reconstructed images showed no sign of damage to the sample.

A later experiment on mimivirus particles at LCLS with shorter pulses (40 fs) at 0.6 nm wavelength, and with a combined analysis of diffraction images and TOF data, creates the basis for **Paper VI**.

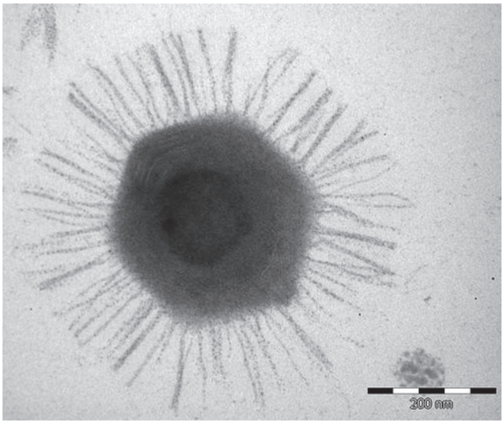

Figure 3.4: Transmission electron micrograph of a mimivirus. The size bar corresponds to 200 nm. (Image from [46]).

3.2.3 Solid samples

The targets used in **Papers II – IV** were bulk solids of niobium (Nb) and vanadium (V). These metals are two of three elemental Type 2 superconductors and - in the case of niobium - are used in the creation of superconducting radio frequency cavities in particle accelerators. Niobium cavities are part of the accelerator setup at FLASH and XFEL [8].

Both niobium and vanadium are efficient hydrogen absorbers and can be used for storage of this element. Using standard techniques [47], the metals can be loaded with hydrogen or deuterium to create hydrogenated or deuterated niobium (NbH, NbD) and vanadium (VH, VD). At atmospheric pressure, the samples are subject to oxidation and will develop a distinct layer of impurities on their surface. With a thickness of a few atomic layers, these impurities prevent the dissipation of hydrogen and deuterium out of the sample. These surface contaminations contain mainly carbon, oxygen, and hydrogen.

For our experiments, polycrystalline Nb and V were doped with deuterium. These samples, together with pure vanadium and monocrystalline niobium, were exposed to intense FEL radiation at FLASH. At a wavelength of 13.5 nm, 15 fs long pulses were focused down to a sub-micron diameter resulting in pulse intensities of $\sim 5 \times 10^{17}$ W/cm^2 on the samples when placed directly into focus. The metals were moved in and out of focus, leading to a change of incident pulse intensity on the sample surface. At positions out of focus, intensities decreased to values as low as $\sim 1 \times 10^{16}$ W/cm^2.

3.3 Simulations

The main method for diagnostics and data acquisition employed in the experiments only captures the aftermath of any photon-material process. Contrary to imaging experiments, where the scattered photon signal is captured on a CCD camera during the pulse, TOF spectra are recorded at a point in time when processes like single photon ionization and subsequent de-excitation have already taken place and long after the sample has turned into a plasma due to the exposure to intense X-ray radiation. However, the spectra encode a lot of information on the interactions. Simulations of the diagnostics and the experimental setup and computational modeling of the relevant processes during and after illumination help to reproduce the experimental findings and understand the underlying dynamics and mechanisms that govern the physical properties of materials. Simulations can also be used to predict interaction processes and the material response to intense radiation by providing theoretical models that can be tested through experiments.

In this work, two simulation tools were used: SIMION, to simulate the behavior of charged particles in electric fields, and CRETIN, to estimate the response of a material to intense FEL radiation.

3.3.1 SIMION

SIMION is a powerful ion and electron simulation software that models the trajectories of charged particles through electric fields in a given geometry [48]. The electric fields are calculated using electrostatic Poisson and Laplace equations, depending on whether space charges are included or not. Boundary conditions constrain the solutions of the electric fields and ensure a good approximation of the experimental setup. They restrict the electric potential to fixed values at specific locations in a simulated geometry. In a TOF spectrometer, voltages on the repeller and extractor plate, as well as the MCP detector and the grounded surface of the field-free drift tube, provide restrictions on the electric potential at these particular locations.

Fig. 3.5 shows the geometry used for simulations in **Paper I**. Ions are created in the interaction region. Specific starting conditions can be selected to emulate the experimental conditions. SIMION calculates the ion response to the electric fields and potentials and follows the resulting trajectories through the entire geometry until the ions impact on the MCP. At the start, end, and intermediate instances of a simulation,

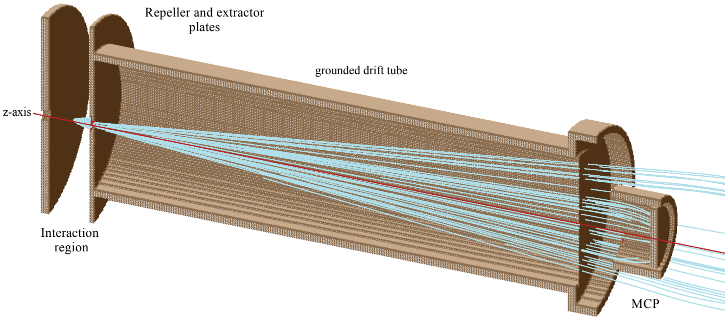

Figure 3.5: Cross-section of the TOF geometry used for SIMION simulations on ion trajectories in **Paper I**. The measurements were performed in active mode. Ions were generated in the interaction region between the repeller and extractor plates and were accelerated towards the MCP detector on the right. An aperture in the extractor limits acceptance into the grounded drift tube. Ion trajectories are depicted in light blue, the red line defines the z-axis of the setup. A thin grid is placed a few mm away in front of the MCP detector to terminate the electric field of the MCP, and keep the drift tube field-free.

information about the ion kinetic energies, flight times, positions in x, y, z, and other ion attributes can be written into an output file. The simulated data can be used to calibrate experimental ion flight times and enable the conversion from flight time to mass-over-charge ratio and ion kinetic energy. SIMION can also be used to test new TOF geometries and predict ion responses.

SIMION was used to simulate ion flight times for the data analysis in **Papers I – VI**. The different TOF spectrometers were calibrated with help of the simulated data and a determination of the kinetic energy distribution from the ion flight times was possible.

3.3.2 CRETIN

Computational modeling was performed with CRETIN [49, 50], a multidimensional non–local thermodynamic equilibrium (NLTE) simulation code for the treatment of physical processes in hot plasmas. It has been successfully shown that it can be used to describe ion displacement and collisions in XFEL experiments on nanocrystals [51]. The materials included in a simulation are detailed in an external file, generally referred to as the atomic model. This file includes information about the level structure and the atomic transition processes to a certain degree of accuracy. Energy levels and transition rates are calculated using a screened hydrogenic model [52, 53]. For simplicity, electron wave functions are assumed to be hydrogen like. The effect of surrounding electrons on any bound electron in the material is calculated using screening constants and an agreement within 25% accuracy is reached with values from the Hartree-Fock-Slater theory [53].

Atomic transition rates and populations, i.e. the atomic kinetics in a plasma, evolve in time, dependent on a range of atomic processes. They are influenced by photon-electron as well as electron-ion, electron-electron, and ion-ion interactions. CRETIN calculates the rates for these processes and determines the different level populations based on the solution of a self-consistent rate equation. A continuum lowering model is applied to account for the lowering of ionization potentials according to the Stewart-Pyatt formula [54]. The atomic kinetics depend strongly on the different temperatures in the sample and therefore, a precise calculation of electron and ion temperatures is needed. Heating rates for temperature adjustments are deduced from the atomic kinetics once atomic population distributions and transition rates have been computed. Furthermore, the results from the atomic kinetics calculations, for example equation of state, opacities, absorption, and emissivities, are used for the evaluation of radiation transport properties, hydrodynamics and other physical processes [55]. The calculation of atomic kinetics, coupled with the description of radiation transport and heat transfer, yields a detailed description of changes in the material during and after the exposure to an intense laser pulse.

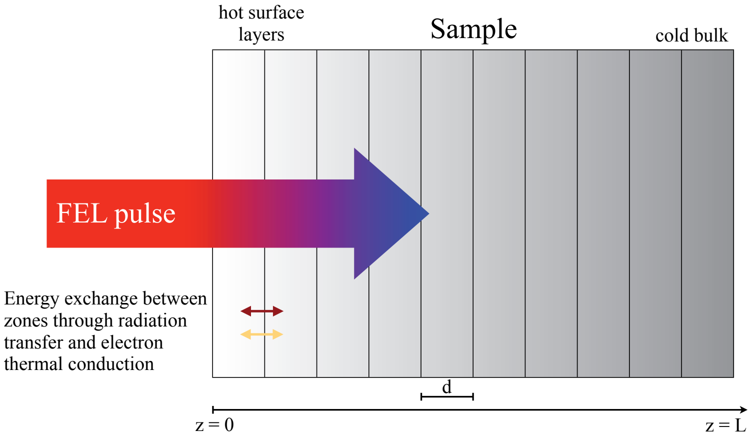

Figure 3.6: Geometrical setup of a 1D simulation on solid material with CRETIN. The material response to intense FEL radiation is simulated over the entire sample of size L which is segmented into zones of equal thickness d. Zones exchange energy in form of radiation (red arrow) and heat transfer (yellow arrow). The laser pulse is incident from the left ($z < 0$).

The approach described here is commonly referred to as the collisional-radiative model. It is the standard model for simulations of NLTE systems. The assumption of NLTE conditions in all papers is justified as the illumination with extremely intense and very short FEL pulses yields rapid changes in electron and ion temperatures and drives the sample far from an equilibrium state.

Simulations on the laser-material interaction in any kind of sample can be performed in 0, 1, 2, or 3 dimensions* with planar or spherical symmetry. Hydrodynamics are only included in 0 and 1D simulations. Fig. 3.6 shows a typical setup for a simulation on a bulk sample in 1D. A material of thickness L is segmented into several zones of equal size d. Material transfer is not possible between these zones but they can exchange energy in form of radiation and heat transfer. CRETIN employs a two-temperature model to calculate the temporal evolution of the ion and electron temperatures. These are used to model heat transfer between zones. The incident radiation is simulated through pulses with either Gaussian or top-hat temporal profiles.

---

*Simulations in 0D represents the response of a sample surface to the incident laser pulse.

4. Results

The development of X-ray FELs made it possible to probe materials under extreme and unprecedented conditions. With intensities closing in on the high-field regime and pulses of femtosecond duration, new and exciting possibilities for experiments become available. Ideas and theories that have been postulated more than a decade ago can now be tested [8].

We performed some of the first experiments at such light sources, exploiting the unique nature of soft and hard X-ray radiation. The interaction dynamics in this short wavelength regime depend not only on the wavelength, pulse intensity, and pulse length of the incident radiation, but also on several material properties, such as size, density, and atomic composition.

In experiments at FLASH and LCLS, we exposed a variety of materials to X-ray pulses at different wavelengths and varying pulse intensities ranging from 10^{13} to well above 10^{17} W/cm^2 to study the damage and explosion dynamics in the samples. These materials include atomic and molecular gases, clusters, complex biological objects relevant to diffraction imaging experiments, and dense bulk solid metals. Data analysis was performed on the recorded TOF spectra and single particle diffraction patterns, and, in the case of solid metals, also on craters formed in the sample surface due to the laser pulses.

4.1 Atoms, molecules, and clusters

Expansion and fragmentation of clusters

Irradiating a cluster with ultrashort and extremely intense FEL radiation results in its complete disintegration. The energy deposition into the material, the ionization, and the charging of the cluster lead to either a Coulomb explosion or a hydrodynamic expansion. In both scenarios, the cluster is obliterated and the signals from charged ionic fragments can be detected. The destruction pathway in the cluster fragmentation depends on the size of the cluster, its composition, and the wavelength, as well as the intensity of the incident radiation pulse. Theoretical studies predict a transition from one expansion mechanism to the other [56].

The disintegration of a cluster through Coulomb explosion is a fast and violent process (tens to hundreds of femtoseconds). In contrast to that, in a hydrodynamic expansion the sample vaporizes on picosecond timescales, as shown by CRETIN simulations. Fig. 4.1 displays how a large methane cluster would burn from the outside towards its center at a constant rate of 0.01 nm/fs. The interior of the cluster is kept together for a longer period of time and the extended lifetime of such a hydrodynamically expanding object allows for additional processes to take place.

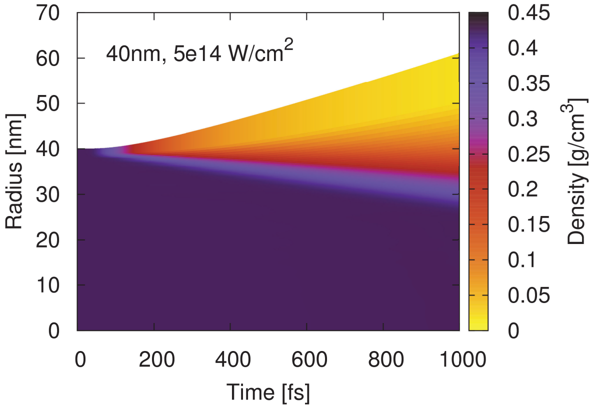

Figure 4.1: Hydrodynamic expansion of a large CH_4 cluster (40 nm radius) irradiated with 15 fs soft X-ray pulses at $\lambda = 13.5$ nm and pulse intensity of 5×10^{14} W/cm^2, as simulated with CRETIN. During a 1 ps simulation the outer layers of the cluster burn off and the remaining core reduces its radius by $\sim$10 nm. This corresponds to an expansion rate of 0.01 nm/fs.

Paper I describes experiments on methane (CH_4) and deuterated methane (CD_4) molecules and clusters. The samples were irradiated with 15 fs soft X-ray pulses, focused down to a spot size of 20 μm, at $\lambda = 13.5$ nm with pulse intensities between 10^{13} and 10^{15} W/cm^2. The results show that the expansion of such complexes has a time- and size-dependent component. Calculations of ion yields for the peaks in the TOF spectra indicate that a transition from Coulomb explosion to hydrodynamic expansion takes place at a cluster size of $\sim 20,000$ molecules per cluster (corresponding radius of 6.7 nm). This transition is tightly coupled to the occurrence of intermediate adducts, namely CH_5^+ and $C_2H_n^+$. Fig. 4.2a shows spectra for molecular CH_4 and for methane clusters containing 20,000 and 100,000 molecules (11.5 nm radius). Apart from an increase in the overall ion signal with cluster size, the spectra also show a size-dependent growth in the ion yield of H^+ and C^+. The dominant feature in these spectra is the appearance of protonated methane (CH_5^+) and higher adducts ($C_2H_n^+$, $n \geq 2$). Their contribution to the overall ion yield changes significantly with cluster size.

The ion yields of CH_5^+ and corresponding higher adducts increase with cluster size up to a radius of 6.7 nm (20,000 molecules per cluster) and then decrease again for larger clusters. The appearance of these adducts can be attributed to molecular recombination between ions and molecules. The change in ion yield with increasing cluster size indicates that additional reaction pathways exist during the expansion of larger clusters through which CH_5^+ and $C_2H_n^+$ can react. This is probably connected to the longevity of larger clusters which increases the probability of collisional processes involving electrons, ions, and molecules. During the slow expansion of a large cluster, more collisions can take place and there is more time for bond formation than during the fast disintegration of a small cluster.

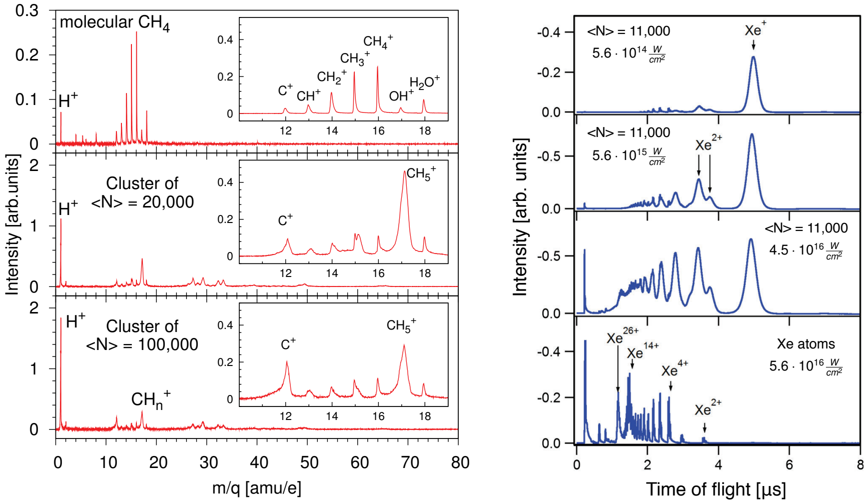

(a) m/q spectra of CH_4 molecules and clusters (b) TOF spectra of Xe atoms and clusters

Figure 4.2: Spectra from CH_4 and Xe clusters. (a) TOF spectra from methane molecules and clusters of different size irradiated with single FEL pulses at $\lambda = 13.5$ nm with an average pulse intensity of 5×10^{14} W/cm^2. The inserts contain a zoom into the region from m/q = 12 to 18. A general increase in H^+ and C^+ peaks with cluster size is visible. Cluster spectra show unique peaks for CH_5^+ and higher adducts that do not occur in the molecular spectrum. (b) TOF spectra of Xe atoms and clusters of fixed size ($\langle N \rangle = 11{,}000$ atoms) irradiated with single pulses at $\lambda = 1.46$ nm and varying pulse intensities. A clear distinction due to the occurrence of various charge states is possible between atomic and cluster spectra.

The above findings are complemented by experiments on xenon clusters described in **Paper V**. Here, xenon clusters containing 11,000 atoms were irradiated with 150 fs long X-ray pulses with $\lambda = 1.46$ nm and pulse intensities between 4×10^{14} W/cm^2 and 6×10^{16} W/cm^2. After the illumination, the cluster disintegrates in a two-step process. First, the positively charged surface layer is expelled in a Coulomb explosion. The remaining cluster core then expands hydrodynamically on a longer timescale. The pressure-driven expansion is due to the formation of a plasma in the cluster, accompanied by three-body recombination which affects the charge state distribution of the ejected ions.

A comparison of TOF spectra from xenon clusters with the spectrum from atomic xenon gas is shown in Fig. 4.2b and displays a significant difference in the charge state distribution. High charge states of xenon up to Xe^{+26} dominate the atomic spectrum whereas low charge states are almost completely absent. These features can be explained through Xe atoms being sequentially ionized by the incident radiation. Ionization to charge states higher than Xe^{+26} requires photon energies of ~ 1440 eV which is well above the energy used (850 eV).

The dominant signal in the spectra of xenon clusters, up to 80% of the total integrated ion signal, comes from ionized xenon with charge states $+1$ to $+6$. Depending on the pulse intensity, higher charge states up to Xe^{+26} were attainable but not to the same level as in atomic xenon. The mean cluster charge was estimated to be $\langle q \rangle = +5$

per xenon atom. The dominance of low charge states in the cluster spectrum can be explained through the formation of a nanoplasma in the illuminated cluster which allows for the occurrence of three-body recombination. This process effectively leads to the formation of lower charge states in the cluster nanoplasma.

Similarly, in **Paper I**, the formation of a hydrodynamically expanding plasma in the cluster core is responsible for the decline in the ion yield of CH_5^+ and $C_2H_n^+$ in larger methane and deuterated methane clusters ($\langle N \rangle \geq 20,000$ molecules). It allows for the occurrence of additional reaction pathways through which these adducts can decay.

Ion acceleration

The fragmentation of a cluster due to illumination with intense X-ray radiation leads to an acceleration of charged particles to high kinetic energies. Ion acceleration was measured in the experiment described in **Paper I**. SIMION simulations of the ion trajectories enabled a conversion from ion flight times to ion kinetic energies. The maximum detected ion energies were determined with 95% confidence level from signal-to-noise ratio calculations.

Ions are expelled from the cluster through Coulomb repulsion as the incident beam rapidly charges the cluster constituents. Ions with small mass, namely H^+ and D^+, are easily repelled by multiply charged heavier ions and are the first to leave the disintegrating cluster. They carry with them information on the early states of the explosion and helps in understanding the dynamics. Fig. 4.3 shows how the ion acceleration is influenced by cluster size and pulse intensity. Depending on the cluster size, kinetic energies of H^+ and D^+ between 50 and 300 eV were measured (Fig. 4.3a). Varying the pulse intensity when illuminating a fixed cluster size shows that ion acceleration and kinetic energy increase with increasing pulse intensity (Fig. 4.3b). H^+ and D^+ ions accelerated to high energies leave the cluster quickly and reduce the amount of positive charges, thus cooling the remaining cluster. The heavier carbon ions experience a less efficient acceleration in the process.

Isotope effect

The measurement of ion acceleration in **Paper I** reveals an effect that has not been observed in this form in previous experiments on clusters at infrared wavelengths [57]. What becomes obvious when looking at Fig. 4.3 is that the acceleration seems to be more efficient for D^+ than for H^+. In all experiments performed on methane and deuterated methane clusters, D^+ ions reached higher maximum kinetic energies compared to H^+. Differences as great as 150 eV were measured (Fig. 4.3a). This kinematic difference is a size-dependent effect as can be seen in Fig. 4.3b, where for larger cluster sizes D^+ ions were systematically accelerated to higher kinetic energies.

The mass difference between hydrogen and deuterium offers an explanation for the observed energy difference. Classical Molecular Dynamics simulations point towards a mass-related kinematic effect in the acceleration of ions from clusters. Due to their heavier mass, D^+ ions are not as quickly expelled from the cluster as H^+ ions. They are inertially confined for a longer time staying close to the rapidly charging core. H^+

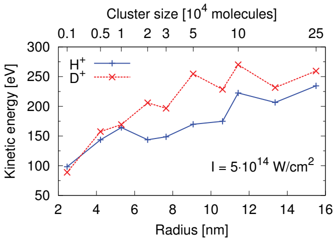

(a) Size dependency

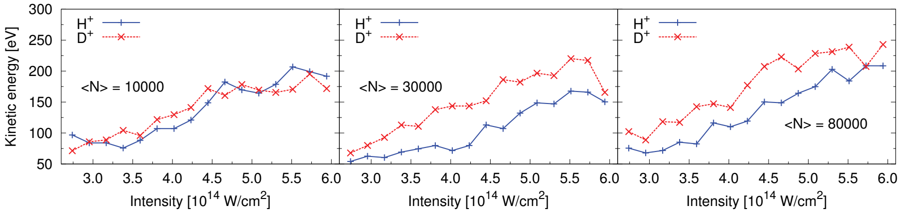

(b) Pulse dependency

Figure 4.3: Ion kinetic energy as a function of cluster size and pulse intensity. (a) Kinetic energy of H^+ and D^+ from CH_4 and CD_4 clusters irradiated with 15 fs long soft X-ray pulses with an average pulse intensity of 5×10^{14} W/cm^2. The kinetic energies show a clear size dependency and increase with cluster size. (b) Kinetic energy of H^+ and D^+ at fixed cluster size for different incident pulse intensities. The energies increase with increasing pulse intensity.

ions escape earlier in the process and do not experience the same repulsive Coulomb potential as D^+. This isotope kinematic effect could be exploited further for inertial confinement studies at X-ray wavelengths.

4.2 Complex biosamples

The results from experiments on clusters are relevant for diffractive imaging experiments on complex biological objects. Knowledge about the explosion dynamics can be used to analyze the behavior of biological samples, like proteins, virus particles, or cells, when exposed to intense X-ray radiation. Similar to the clusters, biological material is destroyed due to the damage induced by the illumination.

In experiments at LCLS, mimivirus particles were injected into the focused X-ray beam. At a wavelength of 0.6 nm, the particles were illuminated by 70 fs long pulses[*] with pulse intensities of up to 5×10^{17} W/cm^2. A CCD detector was used to record the scattered photon signal from the interaction in form of a diffraction pattern. Simultaneously, ions from sample fragmentation were detected with a TOF spectrometer.

Fig. 4.4 shows ion spectra (inverted) and corresponding diffraction patterns for several single mimivirus hits compared to the background signal (on top). The background results from the carrier gas used during the injection of virus particles [7]. A hit is labelled by its event number and the data are sorted according to the strength of

---

[*] 70 fs corresponds to the measurement of the electron bunch. It was shown that this value overestimates the length of the photon pulse which can be approximated to ∼40 fs [26].

a hit. The spectra show features that can be correlated to the incident intensity on the sample. With higher intensities, the first peak, which we associate with a proton signal (H^+), increases drastically and dominates the spectrum. A measure of the scattering strength is also possible with help of the diffraction patterns. The higher the intensity on the sample, the stronger and more intense the scattered signal.

In a diffractive imaging experiment, the CCD detector will be read out regardless of whether a strong or a weak hit has been detected. Weak hits are generally not useful for an image reconstruction to high resolution. During simultaneous measurements of diffraction patterns and ion spectra, the TOF spectrometer could be used as a secondary diagnostic that would give a measure of the strength of a hit, as well as insight into the composition of the sample.

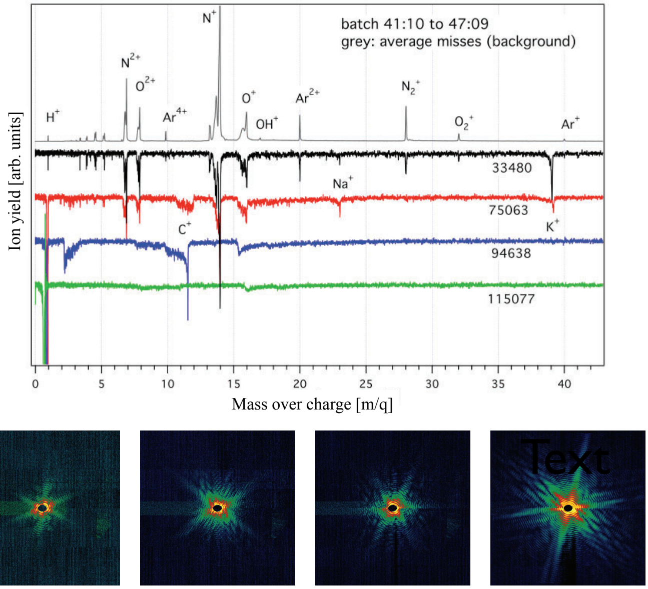

Event #33480 **Event #75063** **Event #94638** **Event #115077**

Figure 4.4: Simultaneous measurement of ion TOF spectra and diffraction patterns of mimivirus particles. Each spectrum (inverted) is associated with a diffraction pattern labelled with the same event number. The scattered intensity increases from event 33480 (black) to 115077 (green). In the spectra, this is accompanied by a significant increase in the proton peak (H^+) and occurrence of ions C^+, Na^+, and K^+. For comparison, the top spectrum shows the background measurements when no particle was hit.

The fastest ions from a sample exposed to intense X-ray radiation leave the sample at an early stage of its expansion. In the case of mimivirus, these fast ions are protons accelerated to kinetic energies of up to 1.5 keV. They carry with them information about the onset of the sample expansion and can reveal details about the explosion dynamics. The maximum ion kinetic energies for every single hit were derived from the leading edge of the proton peak with a 95% confidence level. From the number of scattered photons in each diffraction pattern, one can estimate the incident intensity on the sample, using a simplified scattering model. As displayed in Fig. 4.5a, proton energies are correlated with the calculated number of scattered photons. The energy values are comparable to theoretical values calculated with an isothermal fluid model that was also employed in experiments on solid metals [30].

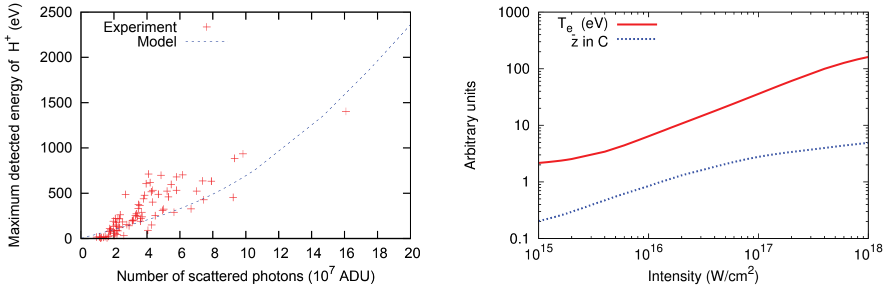

(a) Ion acceleration

(b) Simulations on mimivirus

Figure 4.5: Measurements and simulations on mimivirus in intense X-ray beams. (a) Protons with high kinetic energies are released from the sample at an early stage of the sample expansion. Ion acceleration is tightly coupled to the strength of the interaction, which can be described by the number of scattered photons in a diffraction pattern. The measured proton energies (red crosses) as a function of scattered photons are comparable to theoretical values (blue line). ADU refers to arbitrary detector unit which is proportional to the number of photons in a diffraction pattern. (b) CRETIN simulation of a mimivirus irradiated with intense 50 fs long X-ray pulses at 0.6 nm wavelength with pulse intensities ranging from 10^{15} – 10^{18} W/cm^2. Intense pulses result in higher electron temperatures (T_e) and average ionization ($\bar{z}$) in the sample. T_e and $\bar{z}$ are used to estimate the acceleration of ions at the end of the pulse (Eq. 4.1).

Simulations on the interaction were performed with CRETIN in 1D (Fig. 4.5b). Mimivirus was modeled as a 500 nm sized particle with a sample composition of $H_{23}C_3NO_{10}S$ and density of 1.02 g/cm^3 [58]. Only results from the outermost layer were taken into account for further calculations since the fastest ions are expected to come from the surface of the sample. The incident pulse intensity was varied between 10^{15} W/cm^2 and 10^{18} W/cm^2 to cover the entire range of intensities in the experiment. The more intense the pulse, the more damage is induced in the virus particle in form of ionization and heating. For very intense pulses, ionization in carbon is severe and electron temperatures can reach up to $\sim$ 200 eV. These simulations provide the basis for calculations of the theoretical proton energies shown in Fig. 4.5a. The isothermal fluid model employed here (Eq. 4.1 in 4.3) uses the simulated electron temperature and ionization to calculate theoretical proton energies in Fig. 4.5a.

4.3 Metallic solids

Crater formation

Studies on damage formation in solids have relevance for material science and the design of X-ray optics. At X-ray wavelengths, most materials have a refractive index close to unity, rendering them unpractical for the design of focusing optics. Knowledge of the material response to X-ray exposure and the subsequent damage pathways is essential for finding new material properties and application.

Paper III and **IV** describe the experimental and theoretical examination of ablation and crater formation in bulk solid metals, pure and deuterated niobium and vanadium (Nb, NbD, V, VD). The metals were exposed to 15 fs long soft X-ray pulses focused to a diameter of 800 nm at $\lambda = 13.5$ nm ($E_{ph} = 92$ eV) and with an average pulse energy of 30 μJ. The samples were mounted on a translation stage and moved in and out of the focused beam along the beam direction. In addition to stochastically occurring shot-to-shot variations in the FEL pulse energies, the sample motion along the beam axis resulted in a further variations of the incident pulse intensity on the sample. With the sample positioned in focus, pulse intensities as high as 5×10^{17} W/cm^2 were reached. In comparison, the intensity dropped to 10^{16} W/cm^2 for positions out of focus.

The pulse fluence was well above the ablation thresholds for these materials and the irradiation with a single pulse led to the formation of craters in the sample surface. Fig. 4.6 shows a series of craters in monocrystalline niobium taken at different positions of the metal relative to the focus. Depending on the pulse intensity, craters could reach depths of up to 4.8 μm (in NbD). This is well above the expected absorption length of X-rays at this wavelength ($\sim$ 200 nm for Nb). The depth decreased quickly when moving out of focus.

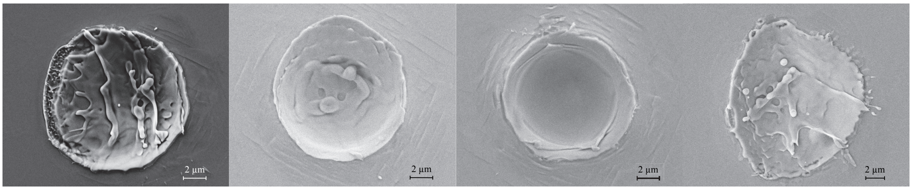

(a) $z = -0.4$ mm (b) $z = -0.2$ mm (c) $z = 0.0$ mm (d) $z = +0.6$ mm

Figure 4.6: SEM images of craters in monocrystalline Nb for different relative sample positions z along the laser. At out-of-focus positions the craters are shallow with depths reaching (a) 2 μm, (b) 3 μm, and (d) 1 μm. The incident pulse intensity in each case is 0.6×10^{17} W/cm^2, 1.1×10^{17} W/cm^2, and 0.4×10^{17} W/cm^2, respectively. (c) At the position of best focus, the crater depth reaches its maximum of 4.4 μm for this material ($I = 2.6 \times 10^{17}$ W/cm^2). The bar corresponds to a length of 2 μm.

The interaction processes in the irradiated material were modeled with CRETIN to compare the measured crater depths to theoretical values (Fig. 4.7). The incident radiation ionizes the solid and increases the density of free electrons. A critical electron density of $N_e \approx 10^{22}$ cm^{-3} is necessary to destabilize the lattice and initiate structural changes [58]. The simulated time evolution of this critical density provides a limit for the theoretical ablation depth in the material. The comparison between the simulated critical ablation depth and the experimental crater depth after 1 ps in Fig. 4.7 shows that at pulse intensities around 10^{16} W/cm^2 the simulated values approach the experimental ones. At higher pulse intensities however, the employed 1D model breaks down and is not able to sufficiently emulate the experimental crater depths.

An explanation for the discrepancy between simulated and experimental crater depths can be found by distinguishing the different contributions to the ablation process. Nonthermal melting is responsible for the initial heating of a sample. Photoionization leads to an increase in N_e. Subsequent material heating is mediated mainly through radiation transport and electron thermal conduction. This occurs on short, sub-picosecond timescales. On timescales longer than 1 ps, hydrodynamic expansion could contribute to an increase in the craters depth. This may be a reason why, for pulse intensities between 10^{16} and 10^{17} W/cm^2, the simulated critical depth underestimates the experimental crater depth.

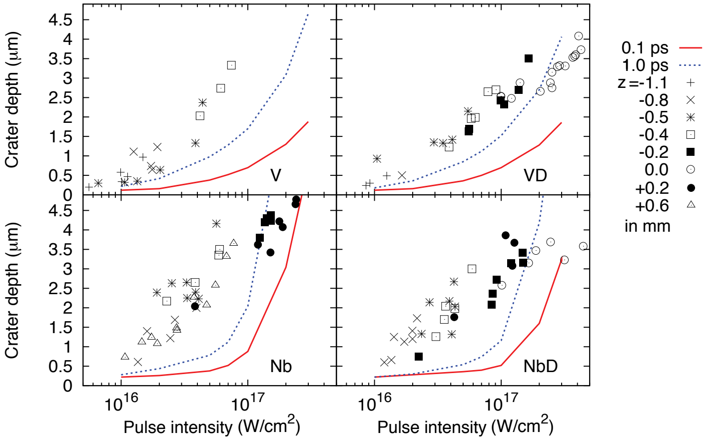

Figure 4.7: Experimental and simulated crater depths as a function of pulse intensity of the incident X-ray pulse. Crater depths were measured with an AFM. The variation in pulse intensity is due to moving the sample through the focus along the beam axis and shot-to-shot fluctuations in the FEL pulses. z shows the sample position relative to the best focus at $z = 0.0$ mm. Simulated critical depths after 0.1 ps (red) and 1 ps (blue) are shown for all irradiated materials. These correspond to the depths where $N_e \approx 10^{22}$ cm^{-3}.

At intensities above 10^{17} W/cm^2, the simulations overestimate the measured values which show signs of saturation. These high intensities facilitate the occurrence of surface transparencies in the material during the short pulse [26]. Rapid ionization of atoms makes them effectively transparent to the incident radiation. The radiation can thus penetrate deeper into the sample, heating the bulk. In the irradiated metals, this would lead to an increase in crater depth. However, the measured depths reach saturation as some of the radiation penetrating to such depths is diluted into a larger surrounding volume and is lost through the sides. Simulations with CRETIN were limited to 1D and did not take into account such energy deposition into the bulk and radiation loss through the sides.

Ion acceleration

Irradiation of solids with short and intense X-ray pulses does not only lead to modifications in the material, like crater formation and ablation. It also results in the acceleration of ions due to charge separation. In the experiment described in **Paper IV** ion TOF spectra were recorded during the illumination of the metal samples. A TOF spectrometer was used in drift mode with an additional high-pass filter to examine specific energy regions and determine the maximum kinetic energies. In combination with SIMION flight time simulations, peak and charge state assignment was possible. The TOF spectra revealed H^+ and D^+ ions with maximum detected kinetic energies of about 5 keV. The heavier metal ions, Nb and V, experienced acceleration of up to 20 keV. Signal-to-noise ratio calculations on the respective peaks in the TOF spectra estimate the maximum kinetic energies at a 95% confidence level. As in the case of ion acceleration in clusters and mimivirus, the first ions to leave the irradiated metals are expelled during the early stages of the sample expansion.

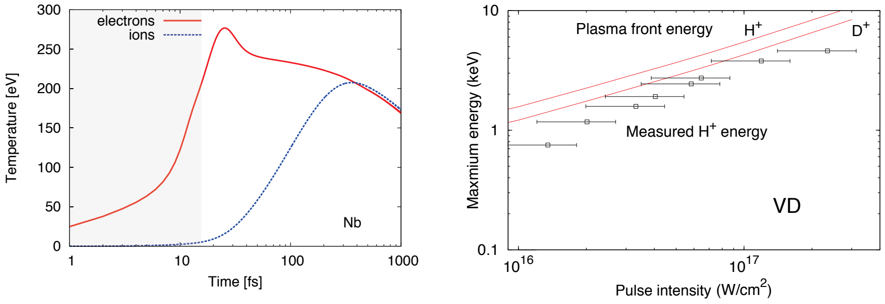

(a) Electron and ion temperatures in niobium

(b) Proton kinetic energies

Figure 4.8: Simulation and experiments on solid metals. (a) Temporal evolution of the simulated electron (T_e) and ion (T_i) temperatures in Nb. Simulations were performed with 15 fs (FWHM) long X-ray pulses (shaded area) at $\lambda = 13.5$ nm and with an intensity of 10^{17} W/cm^2. T_e increases in a direct response to the incident pulse and reaches a maximum shortly after the pulse leaves the sample. Increase in T_i proceeds much slower and approaches a maximum long after the pulse has passed. T_e and T_i equilibrate on a timescale of $\sim$100 – 200 fs. (b) Comparison between the maximum measured proton kinetic energies (H^+) in VD (boxes) and the calculated plasma front energies (Eq. 4.1) for H^+ and D^+ (red lines).

Exposure to intense and short radiation pulses turns the metal samples locally into a plasma. The thermalization processes in this dense, hot plasma were simulated with CRETIN. Ion and electron temperatures equilibrate after $\sim$100 fs (Fig. 4.8a) with ions on the plasma surface reaching temperatures between 100 and 400 eV for pulse intensities above 10^{16} W/cm^2. Fig. 4.8b shows the measured hydrogen kinetic energies, compared to the ion kinetic energies calculated for a plasma front expansion into vacuum. Ions in this plasma front are accelerated according to

$$E_{max} = 2ZT_e \left[\ln \left(\frac{\omega_P t_{acc}}{2\sqrt{2}} \right) - 1 \right]^2 , \tag{4.1}$$

with plasma frequency ω_P, electron temperature T_e, charge state Z, and acceleration time $t_{acc} = 1.3 \times$ FWHM of the laser. These calculations are based on a self-similar isothermal fluid model which models charge separation and the plasma front expansion [53]. The model also predicts maximum energies for highly charged Nb and V ions in the range of 4 – 40 keV, similar to the measured 20 keV for the heavy metal ions.

The ion kinetic energies show signs of saturation for pulse intensities above 10^{17} W/cm^2. As with the saturation in crater depth, this is coupled to the occurring transient surface transparency at such high intensities. Simulations with CRETIN show that the fast ionization of atoms results in a significant drop in absorption at the surface of the plasma. The surface becomes effectively transparent for the incident radiation, leading to saturation in the ion heating and a decline in the ion acceleration efficiency.

Focus determination

In all experiments described in this thesis, knowledge of the incident intensity on the sample surface is crucial. Pulse intensity is calculated based on several beam and experimental setup parameters. Pulse energy and pulse length are a set of fixed beam parameters that are provided by the FEL facility. The focal spot size is a parameter related to the experimental setup and has to be measured individually. A common but time-consuming method for focus determination is the off-line analysis of beam imprints in a suitable material like polymethyl methacrylate (PMMA) [59].

Time is generally scarce during experiments at FELs. In **Paper II** we introduce a rapid in-situ method for focus determination, called "TOF-OFF". The focus position is found through measurements of the kinetic energy of protons accelerated off the surface of a solid sample, as it is moved through the focus.

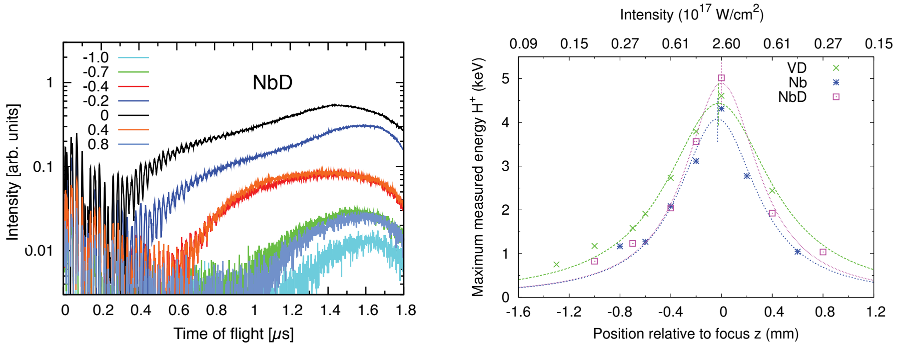

(a) Proton signal from NbD

(b) Maximum proton energies

Figure 4.9: Proton signal as a function of time and maximum proton energies as a function of sample position relative to best focus and pulse intensity. (a) The position with the highest signal intensity and the shortest flight time is labelled as $z = 0.0$ mm and is assumed to be closest to the actual focus z_0 of the incident beam. Moving the sample down- or upstream from this position results in a decrease in signal intensity and a less efficient acceleration of protons. The different curves show positions along the z axis relative to $z = 0.0$ mm. (b) The highest measured proton energies for each sample position show a clear maximum at a sample position equal or close to the actual focus of the beam. A Lorentzian fit to the data shows that the perceived best sample positions for NbD at $z = 0.0$ mm agrees well with the actual focus z_0. In Nb and VD, small differences in the sample placement led to a misalignment by $\sim$30 μm.

The pulse intensity is highest at the position of best focus. TOF spectra show that proton signals are highest and flight times are shortest when the sample is irradiated at a position closest or equal to the best focus position. The shortest flight times in an ion distribution correspond to the highest ion kinetic energies. Fig. 4.9a displays H^+ traces from measurements on deuterated niobium. Each trace was recorded at a different position relative to the beam focus, with $z = 0.0$ labeling the position with the perceived highest yield and shortest flight time. Moving the sample in steps of

200 μm along directions on both sides of the focal plane results in a decrease in both the overall proton yield and kinetic energy.

Further analysis of the proton flight times confirmed that the highest proton kinetic energies were measured for samples positioned close to or at best focus. This is shown in Fig. 4.9b for H^+ kinetic energies from VD, Nb, and NbD. If the incident beam is assumed to be symmetric, a Lorentzian fit to the proton energy data (Fig. 4.9b) can be used to reveal the actual focus position z_0 relative to the sample positions z. The previously assigned best sample position $z = 0.0$ mm agrees well with z_0 in the case of NbD and is off by about 30 μm for VD and Nb.

For most experiments conducted at FEL facilities, high pulse intensities are favorable. **Paper III** and **IV** show that at high enough intensities proton kinetic energies and crater depths show signs of saturation. To avoid a biased focus determination due to saturated energies and crater depths, TOF-OFF can also be conducted with attenuated pulses. The pulse intensity can be reduced in a controlled way, using absorbers in the beamline.

A reliable determination of the focus position is possible with just the measured proton energies. With the TOF-OFF method, the position of the focal plane could be determined with an accuracy of ± 30 μm, a value that is well within the Rayleigh length of the focused FEL beam (± 75 μm) during the experiment.

5. Conclusions

Equipped with a prism and a thermometer, William Herschel stepped into an invisible world in February 1800 when he discovered infrared radiation ("caloric rays"). Invisible light of another type was discovered by Wilhelm Conrad Röntgen a century later with the help of a photographic plate. Today, X-ray pulses from free-electron lasers are so extremely intense that even the simplest measurements require elaborate detection schemes. Results presented in this thesis come from some of the first experiments with X-ray lasers.

The discovery of unusual effects reported in the papers have broad relevance for future studies. The isotope effect and ion acceleration described in **Papers I** and **V**, could be used to accelerate nuclei of heavy hydrogen isotopes to high energies, and ultimately achieve nuclear fusion in clusters. Such a feat has successfully been accomplished in the infrared by others [60]. The mechanisms at play with X-rays are, however, different, and offer new avenues for further studies.

Transiently induced X-ray transparency (**Paper IV**) is a recently discovered phenomenon [25, 26] that leads to saturation in photon absorption, ion acceleration, and ablation. This is relevant for the structural determination of biological materials in coherent X-ray diffraction imaging experiments, where a suppression of photoionization would be beneficial for the integrity of the sample during exposure. The interplay between photoionization, damage, and diffraction quality is outlined in **Paper VI**.

The next years will show a surge in powerful, new X-ray sources that will push the boundaries to new extremes. The European XFEL, LCLS II [61], and the Swiss FEL [62] are some of the upcoming FELs that aim at providing even shorter wavelengths and higher peak brilliance than what currently is available. Improvements in the electron and photon beam parameters, higher intensity pulses, and tighter focusing will enable access to the high-field regime with X-rays. This regime is currently unexplored. At high enough intensities (estimated to start at 10^{22-23} W/cm^2), conditions can be created in which the Keldysh parameter γ is smaller than 1. In this regime, we should be able to create wake fields with GV/cm – TV/cm strengths [63] and observe nonlinear high-field phenomena described in quantum electrodynamics. Such phenomena include the breakdown of vacuum through electron-positron pair production [64] or the emission of Hawking-Unruh radiation [65].

This thesis paves the way to new and exciting experiments at the forefront of photon science. The results could be used to argue a scientific case for building new X-ray lasers such as a Swedish FEL to explore an exciting new world, and give a significant boost to knowledge and understanding.

The possibilities are endless.

6. Sammanfattning på svenska – Summary in Swedish

Osynligt laserljus skapar och undersöker nya former av materia

Upptäckten att det finns ljus utanför det synliga spektret var ett stort vetenskapligt genombrott. Den första personen som steg in i den osynliga världen var William Herschel, år 1800. Han mätte infrarött ljus med bara en termometer och ett prisma. År 1896 passerades nästa milstolpe när Wilhelm Conrad Röntgen oavsiktligt upptäckte röntgenljuset. Under de följande åren har många viktiga vetenskapliga genombrott gjorts som använder detta osynliga ljus. Ett av de viktigaste är användning av röntgenkristallografi, som i mitten av nittonhundratalet bland annat gjorde det möjligt att bestämma strukturen av DNA-molekylen, som bär koden för allt liv. Utveckling och använding av särskilda maskiner som producerar röntgenljus, så kallade synkrotronljuskällor, har möjliggjort studier av strukturen av biologiska molekyler och bidragit med viktig kunskap om livets molekyler.

Den senaste utvecklingen rör användningen av röntgenlasern. Röntgenlasern är en ny ljuskälla som producerar extremt starka och korta röntgenpulser, flera gånger kortare och intensivare än synkrotronljus. Laserpulserna är blixtsnabba - bara några femtosekunder långa. Intensiteten är enorm: om man fokuserar pulserna på en kvadratmikrometer, är intensiteten av röntgenljuset jämförbar med intensiteten av allt solljus som träffar jordytan under samma tid fokuserat på en kvadratmillimeter. Den första lasern, döpt till FLASH, byggdes i Tyskland 2005. Nu finns ett antal anläggningar i världen, LCLS i USA som togs i bruk 2009, Fermi@Elettra i Italien och SACLA i Japan, färdig 2011, samt ett antal som är under konstruktion.

När ett prov träffas av ultrasnabba pulser från en röntgenlaser förstörs provet av energin från strålningen. På kort tid förvandlas provet till plasma och kan nå temperaturer upp till några miljoner grader Celsius. Senare exploderar provet på grund av den extrema tillståndet. Det är viktigt att förstå hur intensiva röntgenpulser växelverkar med materia av olika storlek och komplexitet.

Målet med detta avhandling är att utföra teoretiska och experimentella studier av växelverkan mellan röntgenstrålning och materia. Syftet är att undersöka strålskador på olika prover för att förstå hur jonisering och explosionsdynamik påverkas av energitäthet hos olika former av materia. I ett flertal experiment vid FLASH och LCLS har vi undersökt atomära och molekylära kluster, komplexa virus, och sällsynta jordartsmetaller.

Kluster är små samlingar av materia som kan bestå av några få, upp till flera hundra tusen atomer eller molekyler. Kluster har fördelen att deras storlek och kemiska sammansättning kan kontrolleras under produktionsprocessen. Samtidigt kan kluster användas som enklare modeller för att studera biologiska molekyler och deras beteende i starka röntgenstrålar. Beroende på deras storlek och innehåll, kan kluster explodera snabbt i en våldsam Coulombexplosion, där joner repellerar varandra, eller i en långsammare hydrodynamisk expansion, där alla joner och elektroner kokar tillsammans. Fragment som resulterar från en sådan explosion kan ge information om själva explosionen, ioniseringen och provets innehåll. Vi har upptäckt en dynamisk effekt där tunga väteatomer från ett tungt metankluster kan accelerera snabbare än väteatomer från vanlig metan. Under vissa förhållanden kan en sådan effekt utnyttjas för att accelerera tunga väteatomer så att de kan smälta samman i en energiproducerande kärnfusion.

Kunskap om strålskador är också relevant för studier av komplexa biologiska prover och kan användas för att utveckla metoder för att bestämma strukturen av biologiska prover med röntgenlaser. Detta är speciellt viktigt för prover som inte kan avbildas med konventionella metoder. Framgången med traditionell röntgenkristallografi bygger på att metoden använder kristaller av ett stort antal molekyler. Detta minskar effekten av strålskador, genom att energin fördelas över alla molekyler i kristallen samtidigt som signalen förstärks av det stora antalet molekyler i kristallen. Det finns dock många viktiga biologiska prover som inte kan kristalliseras, eller är extremt strålkänsliga, t. ex. enstaka celler, virus, eller membranproteiner. Med hjälp av röntgenlaser kan man avbilda sådana enskilda prover utan att behöva kristallisera dem. Provet belyses med mycket intensiva och ultrakorta röntgenpulser. Processen är så snabb att signalen kan registreras innan provet förstörts av den intensiva strålningen. Från en sådan diffraktionsbild kan själva strukturen rekonstrueras. Bildens kvalitet och upplösning är beroende av de skador som orsakas av bestrålningen. Förståelse av hur skador induceras av strålning kan hjälpa till att korrigera och förbättra bilden för att nå en bättre upplösning. Vi har studerat hur viruspartiklar exploderar när de träffas av laserpulsen och har undersökt sambandet mellan diffraktionsbilden som ges av pulsen och fragmenteringen av viruspartiklarna som leder till högenergetiska joner.

Steget från biologiska prover till fasta metaller representerar övergången från nano- och mikrovärlden till den makroskopiska världen. På grund av sin storlek förstörs dessa prover inte helt av röntgenstrålningen, men kommer fortfarande att lida lokal skada. När fokuserade laserpulser träffar metallytan bildas kratrar på provets yta genom avlägsnande av material, och detta material kan nå höga kinetiska energier. Vi har upptäckt att materian kan bli nästan genomskinlig för den starka röntgenlasern under korta tider, eftersom atomerna inte hinner absorbera det höga flödet av strålning. Denna fotoabsorption uppvisar mättnad, d.v.s. ju mer energi som absorberas, desto mindre jonisering kan observeras. Dessa studier av fasta material och hur de tål strålning har relevans för att bygga nya och bättre komponeter inom röntgenoptiken.

Resultaten som presenteras i denna avhandling är de första i sitt slag och relevanta för många vetenskapsområden inom fysik, kemi och biologi. Under de kommande åren kommer nya röntgenlaseranläggningar byggas, med högre intensitet och kortare pulser och våglängder än vad som nu är tillgängliga. Utforskning av växelverkan mellan lasern och materia under sådana extrema förhållanden kan potentiellt öppna för banbrytande studier av hittills outforskade fenomen på nano- såväl som på makronivå. Möjligheterna är oändliga.

7. Acknowledgements

Now, let's start with the chapter that will most likely gain the most attention from almost everyone who will get their hands onto this colorful thesis. (I know that I always read this part first, so don't even pretend!)

First and foremost, I have to thank both my supervisors, Janos and Nic:

Nic - for being my walking handbook of all that is physics and answering all my possible and impossible questions, keeping me on track, and telling me to focus. Thank you for many serious and fun discussions about work, life, Romanian corruption, and lots of nerdy things, for teaching me to appreciate the logscale, and reminding me that someone up there in heaven is out to get me and my car. Finally, a big thank you for all your incredible support and help. I hope I didn't do too badly as your first Ph.D. student. As a supervisor, you certainly did well...I mean great!

Janos - for offering me this position during a nightshift at FLASH back in 2007 and telling me to work on the "Project that shall not be named". We've not yet reached the ultimate goal of fusion but we've gotten some great results in the process. During the years, you taught me some valuable lessons, among them: to aim higher than high, to proudly promote my own achievements, and how to correctly observe gorillas (,) using binoculars. Thank you so much for making things possible and for all of the above.

Tomas - for letting me stalk you since our days at SLAC in 2006. Without you mentioning my name during your job presentation I wouldn't be here. Thanks for having impossible discussions on the difference between pasta and noodles, and for cracking bad jokes (Remember though, one joke a day is more than enough!).
Daniel L. - for support, translations, lots of help, and even more fun. Thanks for joining me on the way from pure and young graduate student back in 2007 to old and (hopefully!) wise Ph.D. in 2012.
Jakob - for being one of my past great office mates. Keep that impressive patience of yours. Thanks for company during long beamtime hours, lots of help, and an unforgettable trip to Austin, Texas.
Michiel - for being my current great office mate and trustworthy climbing partner. You made it easy to spot which desk belongs to whom in our office.
Erik - for being a great part-time office mate of mine back in the old days and wearing fancy ties and bow ties. I am still waiting for the leather chaps though.
Martin - for teaching me the difference between a virus and a bacteria. I don't think I will ever forget this because you certainly make sure that I won't!
Calle - for being the only one not giving up on trying to teach me Swedish. I am sorry that it never worked out but I simply don't understand that dialect of yours.
Daniel W. - for always helping me fix my car. Thanks for great office sharing and

company during beamtimes. You were the calmest person around.
Karin - for always using the exact same phrase whenever I ask if you like to have some sushi. I will manage to trick you into saying yes at some point!
Dirk - for long discussions and rants about gaming and games. I hope we'll be able to play through all the ones we talked about.
Dusko - for some entertaining movie afternoons/evenings, great office sharing, and really weird humor.
Max & Gijs - for fun discussions and introducing social activities. Enjoy the next few years until it's your turn to write and defend!
Filipe - for leaving but coming back. We were all eagerly awaiting your return so that you can finally fix our cluster.
Gunilla - for long discussions on a lot of things and company during long evenings in the lab while I was writing this thesis.
Inger - for tasty recipes and tremendous help with making my Swedish readable.

In an order based on the increase of number of letters in a name and reversed alphabetically sorted (because I can), current and former members of this group. Thanks for pleasant, funny, and hilarious coffee breaks, discussions, and the likes: **Sara**, **Olof**, **Rosie**, **Malin**, **Katja**, **Gösta**, **David**, **Marvin**, **Magnus**, **Kerstin**, **Jessica**, **Evalena**, **Claudia**, **Asawari**, **Francesca**, **Charlotte**, **Alexandra**, and everyone else who found his or her way into the lunchroom or my office.

A huge "Thank you!" to the **administrators** who were always eager to help.

Last, but not least: Friends and family who endured and supported me through the last years and decades.
Mom & Dad - for your love and support in all those years. Moving to Sweden wouldn't have been possible without your help.
Ulla & Chris - for telling me back in 2007 that I better not forget to send the invitation for the celebration. Thanks for being proud of me.
Sabina - for always having an open door for me and making me feel at home.
Ute - for letting me make fun of you back when we first met and still talking to me the next time. Thanks for being a great friend, for 'Ofenkäse und Radler', and lots of fun. Wat schön, wat schön!
Beate - for so many years of shared craziness and ultimate fun. For fandubs and singing and watching and gaming. It's been a great time. I also thank you and **Markus** for efficiently distracting me from everything. Thanks for even more gaming, talking, and a lot of questionable and strange humor (Gruppe 4 FTW!).
Tobias - for turning into the greatest friend in the aftermath of a week-long editing session and continuing being one after all those years. I'm very glad to have you!
Karin - for being the best sister ever. Thank you and **Marc** - for constant support, visits, wine, fun, interior design advice, and making me the proud aunt of two adorable but hopelessly spoiled cats.
Ann - for all the mentionable and unmentionable things! Thank you for everything in these last years!

And now you can all head towards page 1 and read the actual thesis.

References

[1] W. Herschel, "Experiments on the refrangibility of the invisible rays of the sun," *Philos. Trans. R. Soc. London*, vol. 90, pp. 284–293, 1800.

[2] W. C. Röntgen, "On a new kind of rays," *Nature*, vol. 53, pp. 274–276, 1896.

[3] Research Collaboratory for Structural Bioinformatics (RSCB) - Protein Data Bank. (www.rscb.org).

[4] F. R. Elder, A. M. Gurewitsch, and R. V. Langmuir, "Radiation from Electrons in a Synchrotron," *Phys. Rev.*, vol. 71, pp. 829–830, 1947.

[5] R. Neutze, R. Wouts, D. van der Spoel, E. Weckert, and J. Hajdu, "Potential for biomolecular imaging with femtosecond X-ray pulses," *Nature*, vol. 406, pp. 752–757, 2000.

[6] N. A. Dyson, *X-Rays in atomic and nuclear physics*. Longman, 1973.

[7] M. M. Seibert, T. Ekeberg, F. R. N. C. Maia, M. Svenda, J. Andreasson, O. Jönsson, D. Odic, B. Iwan, A. Rocker, D. Westphal, M. Hantke, D. P. DePonte, A. Barty, J. Schulz, L. Gumprecht, N. Coppola, A. Aquila, M. Liang, T. A. White, A. Martin, C. Caleman, S. Stern, C. Abergel, V. Seltzer, J.-M. Claverie, C. Bostedt, J. D. Bozek, S. Boutet, A. A. Miahnahri, M. Messerschmidt, J. Krzywinski, G. Williams, K. O. Hodgson, M. J. Bogan, C. Y. Hampton, R. G. Sierra, D. Starodub, I. Andersson, S. Bajt, M. Barthelmess, J. C. H. Spence, P. Fromme, U. Weierstall, R. Kirian, M. Hunter, R. B. Doak, S. Marchesini, S. P. Hau-Riege, M. Frank, R. L. Shoeman, L. Lomb, S. W. Epp, R. Hartmann, D. Rolles, A. Rudenko, C. Schmidt, L. Foucar, N. Kimmel, P. Holl, B. Rudek, B. Erk, A. Hömke, C. Reich, D. Pietschner, G. Weidenspointner, L. Strüder, G. Hauser, H. Gorke, J. Ullrich, I. Schlichting, S. Herrmann, G. Schaller, F. Schopper, H. Soltau, K.-U. Kühnel, R. Andritschke, C.-D. Schröter, F. Krasniqi, M. Bott, S. Schorb, D. Rupp, M. Adolph, T. Gorkhover, H. Hirsemann, G. Potdevin, H. Graafsma, B. Nilsson, H. N. Chapman, and J. Hajdu, "Single mimivirus particles intercepted and imaged with an X-ray laser," *Nature*, vol. 470, pp. 78–81, 2011.

[8] G. Materlik and T. Tschentscher, *TESLA Technical Design Report*. Deutsches Elektronen-Synchrotron DESY, 2001.

[9] J. M. J. Madey, "Stimulated Emission of Bremsstrahlung in a Periodic Magnetic Field," *J. Appl. Phys.*, vol. 42, pp. 1906–1913, 1971.

[10] D. A. G. Deacon, L. R. Elias, J. M. J. Madey, G. J. Ramian, H. A. Schwettman, and T. I. Smith, "First Operation of a Free-Electron Laser," *Phys. Rev. Lett.*, vol. 38, pp. 892–894, 1977.

[11] W. Ackermann, G. Asova, V. Ayvazyan, A. Azima, N. Baboi, J. Baehr, V. Balandin, B. Beutner, A. Brandt, A. Bolzmann, R. Brinkmann, O. I. Brovko, M. Castellano, P. Castro, L. Catani, E. Chiadroni, S. Choroba, A. Cianchi, J. T. Costello, D. Cubaynes, J. Dardis, W. Decking, H. Delsim-Hashemi, A. Delserieys, G. D. Pirro, M. Dohlus, S. Duesterer, A. Eckhardt, H. T.

Edwards, B. Faatz, J. Feldhaus, K. Floettmann, J. Frisch, L. Froehlich, T. Garvey, U. Gensch, C. Gerth, M. Goerlerand, N. Golubeva, H.-J. Grabosch, M. Grecki, O. Grimm, K. Hacker, U. Hahn, J. H. Han, K. Honkavaara, T. Hott, M. Huening, Y. Ivanisenko, E. Jaeschke, W. Jalmuzna, T. Jezynski, R. Kammering, V. Katalev, K. Kavanagh, E. T. Kennedy, S. Khodyachykh, K. Klose, V. Kocharyan, M. Koerfer, M. Kollewe, W. Koprek, S. Korepanov, D. Kostin, M. Krassilnikov, G. Kube, M. Kuhlmann, C. L. S. Lewis, L. Lilje, T. Limberg, D. Lipka, F. Loehl, H. Luna, M. Luong, M. Martins, M. Meyer, P. Michelato, V. Miltchev, W. D. Moeller, L. Monaco, W. F. O. Mueller, O. Napieralski, O. Napoly, P. Nicolosi, D. Noelle, T. Nunez, A. Oppelt, C. Pagani, R. Paparella, N. Pchalek, J. Pedregosa-Gutierrez, B. Petersen, B. Petrosyan, G. Petrosyan, L. Petrosyan, J. Pflueger, E. Ploenjes, L. Poletto, K. Pozniak, E. Prat, D. Proch, P. Pucyk, P. Radcliffez, H. Redlin, K. Rehlich, M. Richter, M. Roehrs, J. Roensch, R. Romaniuk, M. Ross, J. Rossbach, V. Rybnikov, M. Sachwitz, E. L. Saldin, W. Sandner, H. Schlarb, B. Schmidt, M. Schmitz, P. Schmueser, J. R. S. andE. A. Schneidmiller, S. Schnepp, S. Schreiber, M. Seidel, D. Sertore, A. V. Shabunov, C. Simon, S. Simrock, E. Sombrowski, A. A. Sorokin, P. Spanknebel, R. Spesyvtsev, L. Staykov, B. Steffen, F. Stephan, F. Stulle, H. Thom, K. Tiedtke, M. Tischer, S. Toleikis, R. Treusch, D. Trines, I. Tsakov, E. Vogel, T. Weiland, H. Weise, M. Wellhoeffer, M. Wendt, I. Will, A. Winter, K. Wittenburg, W. Wurth, P. Yeates, M. V. Yurkov, I. Zagorodnov, and K. Zapfe, “Operation of a free-electron laser from the extreme ultraviolet to the water window,” *Nat. Photonics*, vol. 1, pp. 336–342, 2007.

[12] P. Emma, R. Akre, J. Arthur, R. Bionta, C. Bostedt, J. Bozek, A. Brachmann, P. Bucksbaum, R. Coffee, F.-J. Decker, Y. Ding, D. Dowell, S. Edstrom, A. Fisher, J. Frisch, S. Gilevich, J. Hastings, G. Hays, P. Hering, Z. Huang, R. Iverson, H. Loos, M. Messerschmidt, A. Miahnahri, S. Moeller, H.-D. Nuhn, G. Pile, D. Ratner, J. Rzepiela, D. Schultz, T. Smith, P. Stefan, H. Tompkins, J. Turner, J. Welch, W. White, J. Wu, G. Yocky, and J. Galayda, “First lasing and operation of an ångstrom-wavelength free-electron laser,” *Nat. Photonics*, vol. 4, pp. 641–647, 2010.

[13] E. A. Schneidmiller and M. V. Yurkov in *Photon beam properties at the European XFEL*, Hamburg: XFEL.EU TN-2011-006, 2011.

[14] H. N. Chapman, A. Barty, M. J. Bogan, S. Boutet, M. Frank, S. P. Hau-Riege, S. Marchesini, B. W. Woods, S. Bajt, R. A. London, E. Plönjes, M. Kuhlmann, R. Treusch, S. Düsterer, T. Tschentscher, J. R. Schneider, E. Spiller, T. Möller, C. Bostedt, M. Hoener, D. A. Shapiro, K. O. Hodgson, D. van der Spoel, F. Burmeister, M. Bergh, C. Caleman, G. Huldt, M. M. Seibert, F. R. Maia, R. W. Lee, A. Szőke, N. Tîmneanu, and J. Hajdu, “Femtosecond diffractive imaging with a soft-x-ray free-electron laser,” *Nat. Phys.*, vol. 2, pp. 839–843, 2006.

[15] E. Allaria, C. Callegari, D. Cocco, W. M. Fawley, M. Kiskinova, C. Masciovecchio, and F. Parmigiani, “The FERMI@Elettra free-electron-laser source for coherent x-ray physics: photon properties, beam transport system and applications,” *New J. Phys.*, vol. 12, pp. 1–17, 2010.

[16] T. Ishikawa, H. Aoyagi, T. Asaka, Y. Asano, N. Azumi, T. Bizen, H. Ego,

K. Fukami, T. Fukui, Y. Furukawa, S. Goto, H. Hanaki, T. Hara, T. Hasegawa, T. Hatsui, A. Higashiya, T. Hirono, N. Hosoda, M. Ishii, T. Inagaki, Y. Inubushi, T. Itoga, Y. Joti, M. Kago, T. Kameshima, H. Kimura, Y. Kirihara, A. Kiyomichi, T. Kobayashi, C. Kondo, T. Kudo, H. Maesaka, X. M. Maréchal, T. Masuda, S. Matsubara, T. Matsumoto, T. Matsushita, S. Matsui, M. Nagasono, N. Nariyama, H. Ohashi, T. Ohata, T. Ohshima, S. Ono, Y. Otake, C. Saji, T. Sakurai, T. Sato, K. Sawada, T. Seike, K. Shirasawa, T. Sugimoto, S. Suzuki, S. Takahashi, H. Takebe, K. Takeshita, K. Tamasaku, H. Tanaka, R. Tanaka, T. Tanaka, T. Togashi, K. Togawa, A. Tokuhisa, H. Tomizawa, K. Tono, S. Wu, M. Yabashi, M. Yamaga, A. Yamashita, K. Yanagida, C. Zhang, T. Shintake, H. Kitamura, and N. Kumagai, "A compact X-ray free-electron laser emitting in the sub-ångström region," *Nat. Photonics*, vol. 6, pp. 540–544, 2012.

[17] DESY - FLASH. (flash.desy.de).

[18] A. Lindblad, S. Svensson, and K. Tiedtke, *A compendium on beam transport and beam diagnostic methods for Free Electron Lasers*. Deutsches Elektronen-Synchrotron DESY, 2011.

[19] M. Protopapas, C. H. Keitel, and P. L. Knight, "Atomic physics with super-high intensity lasers," *Rep. Prog. Phys.*, vol. 60, pp. 389–486, 1997.

[20] D. Attwood, *Soft X-rays and extreme ultraviolet radiation*. Cambridge University Press, 1999.

[21] S. P. Hau-Riege, *High-Intensity X-rays – Interaction with Matter*. Wiley-VCH, 2011.

[22] P. Persson, S. Lunell, A. Szőke, B. Ziaja, and J. Hajdu, "Shake-up and shake-off excitations with associated electron losses in x-ray studies of proteins," *Prot. Sci.*, vol. 10, pp. 2480–2484, 2001.

[23] B. Ziaja, R. A. London, and J. Hajdu, "Unified model of secondary electron cascades in diamond," *J. Appl. Phys.*, vol. 97, pp. 064905/1–9, 2005.

[24] F. F. Chen, *Introduction to plasma physics and controlled fusion*. Plenum Press, 1984.

[25] B. Nagler, U. Zastrau, R. R. Faeustlin, S. M. Vinko, T. Whitcher, A. J. Nelson, R. Sobierajski, J. Krzywinski, J. Chalupský, E. Abreu, S. Bajt, T. Bornath, T. Burian, H. Chapman, J. Cihelka, T. Doeppner, S. Duesterer, T. Dzelzainis, M. Fajardo, E. Foerster, C. Fortmann, E. Galtier, S. H. Glenzer, S. Goede, G. Gregori, V. Hájková, P. Heimann, L. Juha, M. Jurek, F. Y. Khattak, A. R. Khorsand, D. Klinger, M. Kozlova, T. Laarmann, H. J. Lee, R. W. Lee, K.-H. Meiwes-Broer, P. Mercere, W. J. Murphy, A. Przystawik, R. Redmer, H. Reinholz, D. Riley, G. Roepke, F. Rosmej, K. Saksl, R. Schott, R. Thiele, J. Tiggesbaeumker, S. Toleikis, T. Tschentscher, I. Uschmann, H. J. Vollmer, and J. S. Wark, "Turning solid aluminium transparent by intense soft X-ray photoionization," *Nature Physics*, vol. 5, pp. 693–696, SEP 2009.

[26] L. Young, E. P. Kanter, B. Kraessig, Y. Li, A. M. March, S. T. Pratt, R. Santra, S. H. Southworth, N. Rohringer, L. F. DiMauro, G. Doumy, C. A. Roedig, N. Berrah, L. Fang, M. Hoener, P. H. Bucksbaum, J. P. Cryan, S. Ghimire, J. M. Glownia, D. A. Reis, J. D. Bozek, C. Bostedt, and M. Messerschmidt, "Femtosecond electronic response of atoms to ultra-intense x-rays," *Nature*, vol. 466, pp. 56–66, 2010.

[27] D. von der Linde, K. Sokolowski-Tinten, and J. Bialkowski, "Laser-solid interaction in the femtosecond time regime," *Appl. Surf. Sci.*, vol. 109-110, pp. 1–10, 1997.

[28] K. Sokolowski-Tinten, J. Bialkowski, A. Cavalleri, and D. von der Linde, "Transient States of Matter during Short Pulse Laser Ablation," *Phys. Rev. Lett.*, vol. 81, pp. 224–227, 1998.

[29] J. Chalupský, L. Juha, V. Hájková, J. Cihelka, L. Vysin, J. Gautier, J. Hajdu, S. P. Hau-Riege, M. Jurek, J. Krzywinski, R. A. London, E. Papalazarou, J. B. Pelka, G. Rey, S. Sebban, R. Sobierajski, N. Stojanovic, K. Tiedtke, S. Toleikis, T. Tschentscher, C. Valentin, H. Wabnitz, and P. Zeitoun, "Non-thermal desorption/ablation of molecular solids induced by ultra-short soft x-ray pulses," *Opt. Express*, vol. 17, pp. 208–217, 2009.

[30] P. Mora, "Plasma Expansion into a Vacuum," *Phys. Rev. Lett.*, vol. 90, pp. 185002/1–4, 2003.

[31] H. Schwoerer, S. Pfotenhauer, O. Jäckel, K.-U. Amthor, B. Liesfeld, W. Ziegler, R. Sauerbrey, K. W. D. Ledingham, and T. Esirkepov, "Laser-plasma acceleration of quasi-monoenergetic protons from microstructured targets," *Nature*, vol. 439, pp. 445–448, 2006.

[32] M. M. Seibert, S. Boutet, M. Svenda, T. Ekeberg, F. R. N. C. Maia, M. J. Bogan, N. Tîmneanu, A. Barty, S. Hau-Riege, C. Caleman, M. Frank, H. Benner, J. Y. Lee, S. Marchesini, J. W. Shaevitz, D. A. Fletcher, S. Bajt, I. Andersson, H. N. Chapman, and J. Hajdu, "Femtosecond diffractive imaging of biological cells," *J. Phys. B: At. Mol. Opt. Phys*, vol. 43, pp. 194015/1–9, 2010.

[33] J. J. Thompson, "Rays of positive electricity," *Proc. Phys. Soc. London, Sec. A*, vol. 89, pp. 1–20, 1913.

[34] M. Guilhaus, "Principles and Instrumentation in Time-of-flight Mass Spectrometry," *J. Mass Spectrom.*, vol. 30, pp. 1519–1532, 1995.

[35] E. W. Becker, K. Bier, and W. Henkes, "Strahlen aus kondensierten Atomen und Molekülen im Hochvakuum," *Z. Physik*, vol. 146, pp. 333–338, 1956.

[36] O. F. Hagena, "Nucleation and growth of clusters in expanding nozzle flows," *Surface Science*, vol. 106, pp. 101–116, 1981.

[37] R. L. Johnston, *Atomic and molecular clusters*. Taylor and Francis, 2002.

[38] B. Hess, C. Kutzner, D. van der Spoel, and E. Lindahl, "GROMACS 4: Algorithms for Highly Efficient, Load-Balanced, and Scalable Molecular Simulation," *J. Chem. Theory Comput.*, vol. 4, pp. 435–447, 2008.

[39] O. F. Hagena and W. Obert, "Cluster formation in expanding supersonic jets - Effect of pressure, temperature, nozzle size, and test gas," *J. Chem. Phys.*, vol. 56, pp. 1793–1802, 1972.

[40] K. W. Madison, P. K. Patel, D. Price, A. Edens, M. Allen, T. E. Cowan, J. Zweiback, and T. Ditmire, "Fusion neutron and ion emission from deuterium and deuterated methane cluster plasmas," *Phys. Plas.*, vol. 11, no. 1, pp. 270–277, 2004.

[41] M. Rutzen, S. Kakar, C. Rienecker, R. von Pietrowski, and T. Möller, "Cluster aggregation: a new method for producing atomic and molecular clusters," *Z. Phys. D*, vol. 38, pp. 89–90, 1996.

[42] B. La Scola and S. Audic and C. Robert and L. Jungang and X. de Lamballerie and M. Drancourt and R. Birtles and J. M. Claverie and D. Raoult, "A Giant

Virus in Amobae," *Science*, vol. 299, p. 2033, 2003.

[43] J. M. Claverie and C. Abergel, "Mimivirus and its virophage," *Annu. Rev. Genet.*, vol. 43, pp. 49–66, 2009.

[44] B. La Scola and C. Desnues and I. Pagnier and C. Robert and L. Barrassi and G. Fournous and M. Merchat and M. Suzan-Monti and P. Forterre and E. Koonin and D. Raoult, "The virophage as a unique parasite of the giant mimivirus," *Nature*, vol. 455, pp. 100–104, 2004.

[45] C. Xiao, Y. G. Kuznetsov, S. Sun, S. L. Hafenstein, V. A. Kostyuchenko, P. R. Chipman, M. Suzan-Monti, D. Raoult, A. McPherson, and M. G. Rossmann, "Structural studies of the giant mimivirus," *PLoS Biol.*, vol. 7, pp. 958–966, 2009.

[46] D. Raoult and B. La Scola and R. Birtles, "The Discovery and Characterization of Mimivirus, the Largest Known Virus and Putative Pneumonia Agent," *Clin. Infect. Dis.*, vol. 45, pp. 95–102, 2007.

[47] G. K. Pálsson, A. R. Rennie, and B. Hjörvarsson, "Examination of the reliability of x-ray techniques for determining hydrogen-induced volume changes," *Phys. Rev. B*, vol. 78, pp. 104118/1–7, 2008.

[48] D. A. Dahl, "SIMION for the personal computer in reflection," *Int. J. Mass Spectrom.*, vol. 200, pp. 3–25, 2000.

[49] H. A. Scott, "Cretin - a radiative transfer capability for laboratory plasmas," *J. Quant. Spectrosc. Radiat. Transf.*, vol. 71, pp. 689–701, 2001.

[50] H. A. Scott and S. B. Hansen, "Advances in NLTE modeling for integrated simulations," *High Energy Density Phys.*, vol. 6, pp. 39–47, 2010.

[51] A. Barty, C. Caleman, A. Aquila, N. Tîmneanu, L. Lomb, T. A. White, J. Andreasson, D. Arnlund, S. Bajt, T. R. M. Barends, M. Barthelmess, M. J. Bogan, C. Bostedt, J. D. Bozek, R. Coffee, N. Coppola, J. Davidsson, D. P. DePonte, R. B. Doak, T. Ekeberg, V. Elser, S. W. Epp, B. Erk, H. Fleckenstein, L. Foucar, P. Fromme, H. Graafsma, L. Gumprecht, J. Hajdu, C. Y. Hampton, R. Hartmann, A. Hartmann, G. Hauser, H. Hirsemann, P. Holl, M. S. Hunter, L. Johansson, S. Kassemeyer, N. Kimmel, R. A. Kirian, M. Liang, F. R. N. C. Maia, E. Malmerberg, S. Marchesini, A. V. Martin, K. Nass, R. Neutze, C. Reich, D. Rolles, B. Rudek, A. Rudenko, H. Scott, I. Schlichting, J. Schulz, M. M. Seibert, R. L. Shoeman, R. G. Sierra, H. Soltau, J. C. H. Spence, F. Stellato, S. Stern, L. Strüder, J. Ullrich, X. Wang, G. Weidenspointner, U. Weierstall, C. B. Wunderer, and H. N. Chapman, "Self-terminating diffraction gates femtosecond X-ray nanocrystallography measurements," *Nat. Photonics*, vol. 6, pp. 35–40, 2012.

[52] J. C. Slater, "Atomic Shielding Constants," *Phys. Rev.*, vol. 36, pp. 57–64, 1930.

[53] R. More, "Electronic energy-levels in dense plasmas," *J. Quant. Spectrosc. Radiat. Transf.*, vol. 27, pp. 345–357, 1982.

[54] J. C. Stewart and K. D. Pyatt, "Lowering of ionization potentials in plasmas," *Astrophys. J.*, vol. 144, pp. 1203–1211, 1966.

[55] H. A. Scott and R. W. Mayle, "GLF - A Simulation Code for X-Ray Lasers," *Appl. Phys. B.*, vol. 58, pp. 35–43, 1994.

[56] B. Ziaja, H. Wabnitz, F. Wang, E. Weckert, and T. Möller, "Energetics, Ionization and Expansion Dynamics of Atomic Clusters Irradiated with Short Intense Vacuum-Ultraviolet Pulses," *PRL*, vol. 102, pp. 205002/1–4, 2009.

[57] M. Hohenberger, D. R. Symes, K. W. Madison, A. Sumeruk, G. Dyer, A. Edens, W. Grigsby, G. Hays, M. Teichmann, and T. Ditmire, “Dynamic Acceleration Effects in Explosions of Laser-Irradiated Heteronuclear Clusters,” *Phys. Rev. Lett.*, vol. 95, pp. 195003/1–4, 2005.

[58] M. Bergh, N. Tîmneanu, S. P. Hau-Riege, and H. A. Scott, “Interaction of ultrashort x-ray pulses with B_4C, SiC, and Si,” *Phys. Rev.* **E**, vol. 77, pp. 026404/1–8, 2008.

[59] J. Chalupský, L. Juha, J. J. Cihelka, V. Hájková, S. Koptyaev, J. Krása, A. Velyhan, M. Bergh, C. Caleman, J. Hajdu, R. M. Bionta, H. Chapman, S. P. Hau-Riege, R. A. London, M. Jurek, J. Krzywinski, R. Nietubyc, J. B. Pelka, R. Sobierajski, J. M. ter Vehn, A. Tronnier, K. Sokolowski-Tinten, N. Stojanovic, K. Tiedtke, S. Toleikis, T. Tschentscher, H. Wabnitz, and U. Zastrau, “Characteristics of focused soft X-ray free-electron laser beam determined by ablation of organic molecular solids,” *Opt. Expr.*, vol. 15, pp. 6036–6043, 2007.

[60] T. Ditmire, J. Zweiback, V. O. Yanovsky, T. E. Cowan, G. Hays, and K. B. Wharton, “Nuclear fusion from explosions of femtosecond laser-heated deuterium clusters,” *Nature*, vol. 398, pp. 489–492, 1999.

[61] SLAC National Accelerator Center - LCLS II. (https://slacportal.slac.stanford.edu/sites/lcls_public/lcls_ii/Pages/default.aspx).

[62] Paul Scherrer Institute - Swiss FEL. (http://www.psi.ch/swissfel/).

[63] T. Tajima, “Fundamental physics with an x-ray free electron laser,” *Plasma Phys. Rep.*, vol. 29, pp. 231–235, 2003.

[64] A. Ringwald, “Pair production from vacuum at the focus of an x-ray free electron laser,” *Phys. Lett.*, vol. 510, pp. 107–116, 2001.

[65] W. Unruh, “Notes on black-hole evaporation,” *Phys. Rev. D*, vol. 14, pp. 870–892, 1976.

ACTA
UNIVERSITATIS
UPSALIENSIS
UPPSALA
2012

Distribution: publications.uu.se
urn:nbn:se:uu:diva-180997